공학박사 학위논문

Dynamic thermo-optic modulation using vanadium dioxide based phase-transition gratings

바나듐 이산화물 기반 상변이 격자들을

이용한 능동 열광학 변조

2019년 2월

서울대학교 대학원

전기·정보공학부

김 선 제

Abstract

Dynamic thermo-optic modulation using vanadium dioxide based phase-transition gratings

Sun-Je Kim

Department of Electrical and Computer Engineering

College of Engineering

Seoul National University

For the last two decades, various nanophotonic devices have been developed in the fields of plasmonics and metamaterials. There are two main goals of the nanophotonic devices in the fields. One is to confine light on metallic surface and manipulate it in subwavelength scale beyond the diffraction limit. The second is to design artificial materials with extraordinary optical properties that do not exist in the nature. Nanophotonics community has been trying to achieve such phase goals for next-generation miniaturized and integrated optical systems. In particular, dynamically tunable nanophotonic devices have been in spotlight and demonstrated by combining dynamically reconfigurable optical materials and periodic optical grating structures. Optical responses of such devices can be tuned dynamically by application of external stimuli such as heat, voltage, current, and optical pulse.

Recently, the representative insulator-to-metal phase-transition material responsive to thermal stimulus, vanadium dioxide, has been thoroughly studied for optical applications. Vanadium dioxide is advantageous in manipulating the visible, near-infrared, and infrared light by virtue of the large change of the dielectric function.

This dissertation proposes the novel nanophotonic engineering methods of combining optical grating structures and vanadium dioxide for dynamic,

extraordinary thermo-optic modulation of light scattering. Specifically, momentum, intensity, color spectrum, and polarization state of scattered light are modulated based on the transition characteristics of vanadium dioxide and periodic grating functionalities in the visible and near-infrared. Every main chapters present the theoretical and numerical studies involving effects of optical grating geometry for the certain intended modulation functions.

In the first chapter, the concepts of dynamic nanophotonics are introduced. In addition, wavelength-dependent optical properties of vanadium dioxide are discussed with experimental studies.

In the second chapter, nanophotonic phase-transition switch is proposed for asymmetric excitation and dynamic directivity switching of surface plasmon polaritons. The vanadium dioxide metagrating is demonstrated as the directional switch using thermally switchable asymmetric unit cell and grating period-assisted momentum matching of surface plasmon polaritons.

The third chapter introduce the broadband efficient modulation method of transmissivity with vanadium dioxide diffraction grating. Rather than using subwavelength-spaced resonant metasurfaces, diffractive large period grating is designed for broadband operation. Based on such diffraction modulation, forward transmissivity is largely modulated with high efficiency over the broad bandwidth in the near-infrared.

In the fourth chapter, the deep subwavelength-spaced gratings, reflective metafilms, are proposed by introducing mirror and effective medium approximation for efficient operation in the visible spectrum. For high contrast modulation of visible light color spectrum, near-unity absorption is designed in noble metal-vanadium dioxide metafilm and tuned owing to large anisotropy and boosted phase-transition effect. Moreover, dynamic polarization modulation is achieved by virtue of extremely anisotropic tunability of absorptions dips.

At last, conclusion is presented with brief summary and discussions. The results of the dissertation would help developing and improving next-generation optical switch, ultracompact display pixel, and high performance spatial light modulators in the future.

Keywords: Nanophotonics, dynamic light modulation, phase-transition material, vanadium dioxide, metamaterial, nanophotonic grating
Student Number: 2014-21652

Contents

List of Tables

List of Figures

Chapter 1 Introduction

1.1 Overview of dynamic nanophotonics

Nanophotonics community has been focused on exploring subwavelength optical phenomenon and development of optical nanoscale devices with extraordinary functions. Design of extraordinary optical scattering and modulation of various properties of scattered light are the main themes of nanophotonics [1, 2]. In particular, plasmonics and metamaterials have been the main topics for the last two decades. Plasmonics deals with surface plasmon polaritons (SPPs) which are the quasi-particles launched by momentum-matched coupling between surface electron current on metallic surface and light at frequencies under the plasma frequency [1, 3-5]. By converting free space light into SPPs confined beyond the diffraction limit, it is possible to manipulate light with nanoscale structures with high index contrast. On the other hand, metamaterial is the field focusing on extraordinary bulk optical properties of artificial materials which are not present in the nature [2, 6]. By designing subwavelength-spaced periodic arrangement and shape of nanoscale unitcells, effective homogeneous optical

properties can be designed at will. For example, negative refraction of light and cloaking has been achieved in part [7, 8].

Among various efforts to develop nanophotonics devices and systems in both plasmonics and metamaterial fields, reconfigurable optical devices with reconfigurable optical materials (ROMs) have been in the spotlight even though it is extremely challenging to be demonstrated with high performance. The field involving such challenges is called dynamic nanophotonics [9, 10]. Scattering properties are modulated by changing dielectric functions of ROMs included in dynamic nanophotonic devices when external stimuli are applied on them. The key technological issue of dynamic nanophotonics is to design geometric structures combining nanophotonic structures and ROMs. Thus, both design of nanophotonic structures and selection of proper ROMs are significant.

Relation between period of nanophotonic structure and operation wavelength is the critical issue in nanophotonics field for solving scattering problems in various configurations and environments according to the scattering characteristics at certain distance of interest [11]. Especially, when scale of period is comparable to optical wavelength, both period and subwavelength-sized unitcell also called nanoantenna [11, 12] determine the optical response of device.

When a period of nanophotonic grating structure is larger than a wavelength, incident light is diffracted into discrete output channels ruled by momentum matching principle depending on wavelength. This principle originates from linear eigenvalue problem of wave optics when complete periodicity is given into light wave-matter interaction [13]. The specific diffraction condition in a two dimensional configuration with one dimensional periodic grating can be expressed analytically as follows.

$$n_o \sin\theta_o = n_i \sin\theta_i + m\frac{\lambda}{\Lambda}. \qquad (1.1)$$

Here, θ_o, θ_i, m, λ, and Λ denote output diffraction angle, illumination angle, integer valued discrete diffraction order, wavelength, and grating period, respectively. n_o and n_i are refractive indices of output and input sides, respectively. $m = 0$ indicates diffraction-free Snell's refraction law. On the other hand, in non-zero m cases, as wavelength and period are comparable, large diffraction angle is achieved. It enables building various optical information processing systems with compact decomposition and manipulation of optical signal.

However, distribution of input power into the permitted diffraction channels and overall radiation pattern are not determined by the above momentum matching condition. It depends on designing material property, shape of unitcell nanoantenna structure, and illumination conditions.

When grating period becomes smaller than wavelength, free space diffraction is restricted and only allowed diffraction channel is $m = 0$ according to Equation (1.1). This kind of arrangement is called subwavelength spacing. If a subwavelength-spaced optical grating has thin thickness comparable to wavelength, the optical grating is also called optical metasurface. In this regime, scattering properties of a metasurface are determined dominantly by individual nanoantenna geometries and indiex contrasts of them [11]. If a metallic plane is located near a such metasurface for transverse magnetic (TM) illumination, diffraction into SPPs could be possible [1].

On the other hand, when a period decreases much smaller than the half of wavelength, light experiences an effective homogeneous material (metamaterial or metasurface) with an effective refractive index tensor [6]. Thus, a grating can be modelled as an effective homogeneous dielectric slab. Thus, as interaction between light and grating varies largely mainly according to grating period, it is essential to concern about proper period regime and corresponding physics for demonstration of intended light scattering aspects ahead of what kind of ROM is chosen for modulation.

Electrical, thermal, and optical energy can tune dielectric functions of ROMs such as graphene [14], transparent conducting oxides (TCOs) [15],

chemically active materials [16, 17], and phase-transition materials (PTMs) [18-20] working in optical frequency regime. However, they differ mainly in terms of tunability of dielectric function, area of tunable region, and operating frequency regime.

Dielectric functions of graphene and TCOs can be controlled by external voltage in various capacitive schemes in the infrared (IR) and near-infrared (NIR). Thus, fast modulation can be achieved. However, active tunable regions of graphene and TCOs are extremely thin. Their thicknesses are about 1 nm and few nanometers, respectively. Hence, it is essential to enhance interactions between light-ultrathin active regions of them to modulate light scattering with high contrast. Previous studies achieve the enhancement via densely arranged, subwavelength-spaced metasurfaces with resonant electromagnetic field confinement so that resonant bandwidth-limited tunability is achieved. Moreover, their tunability is suppressed intrinsically in the visible and NIR range despite introduction of the nanophotonic resonances.

Oxidation and reduction of Mg are the representative phenomena inducing dielectric function change studied recently [16, 17]. Chemical reactions of Mg can change resonant optical scatterings largely with high resolution when they are combined with resonant metasurface strategies.

However, such chemically active material is also limited in terms of active regions and low modulation speed.

On the other hand, PTMs including VO_2 [18], $Ge_2Sb_2Te_5$ [19], and $SmNiO_3$ [20] are advantageous in tunability bandwidth including from the visible to IR, fast modulation method, and large tunability of dielectric function without restriction of active region. Especially, VO_2, a volatile continuously changing PTM, can be easily modulated with largely tunable optical responses in the visible and NIR. These advantages of VO_2 make it a powerful ingredient for building nanophotonic active applications for display and communications. In the following section, phase-transition properties of VO_2 are introduced with experimental results. Especially, reconfigurable optical properties of it are discussed thoroughly when it is actively tuned by thermal stimulus around the critical temperature (~341 K).

1.2 VO_2: a volatile phase-transition material

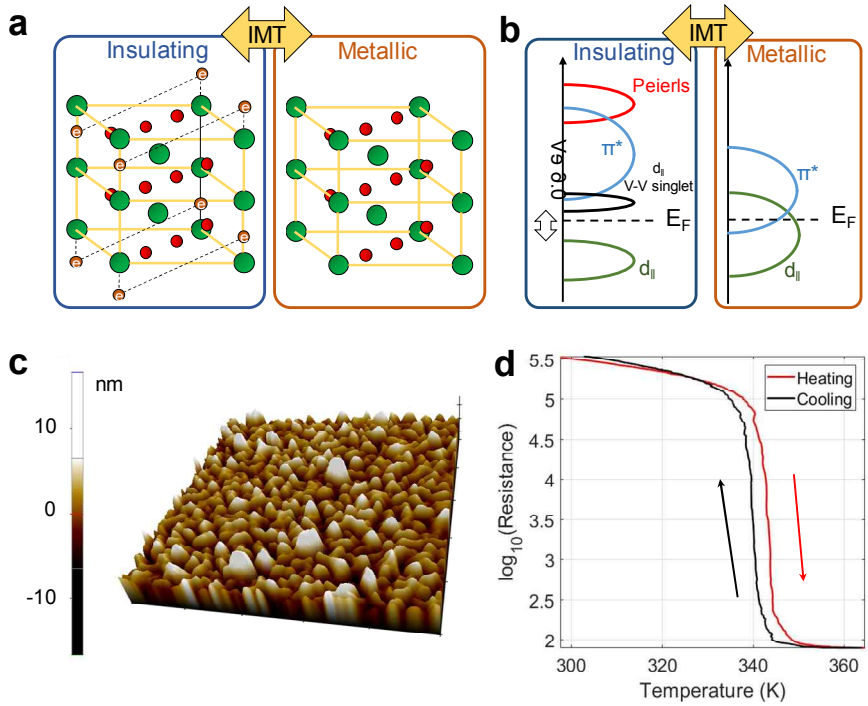

Figure 1.1.1 (a) Schematic description of the molecular structure change and (b) schematic description of the electronic band structures and density of states driven by the IMT of VO_2. Green and red spheres in (a) imply vanadium and oxygen atoms, respectively. (c) Atomic force micrograph of VO_2 film surface. (d) Temperature-dependent cyclic transition of VO_2 film resistance.

VO_2 has attracted much interest from the various research communities ranging from condensed matter physics to electronics in recent decades. The

fascinating key advantage of VO_2 is easily achievable tunability of electronic, electric, and optical properties around moderate critical temperature about 341 K. The brief analysis of the IMT of VO_2 can be understood in terms of change in molecular and electronic band structure. Figure 1.1(a) presents that the low temperature insulating phase and the high temperature metallic phase correspond to monoclinic (M_1) and rutile lattice structures, respectively. As shown in Figure 1.1(b), in the insulating phase, semiconductor-like band structure is shown as a result of splitting of $3d_{\|}$ electron energy band owing to V-V dimerization. The bandgap about 0.6 eV has been verified [18]. On the other hand, when the temperature goes up over the critical temperature, the splitted $3d_{\|}$ bands are degenerated and the band structure is converted with disappearance of the bandgap while the unitcell changes into rutile one [Figures 1.1(a and b)].

VO_2 film is fabricated by the conventional pulsed-laser deposition (PLD) (LAMBDA PHYSIK, COMPEX 205) with a KrF excimer laser at 248 nm [21] on c-plane sapphire substrate. The surface property is characterized with grain imaging conducted using atomic force microscopy (Park Systems, XE150) [Figure 1.1(c)]. The roughness shows a Gaussian distribution with standard deviation about 3 nm when the thickness of the film is about 40 nm. Grain size and surface roughness of PLD-grown VO_2 increase when the

deposition time and thickness increases. The most interesting material property of VO_2 is the giant change of electrical resistance and conductivity [Figure 1.1(e)]. Figure 1.1(d) shows the reversible measurement of PLD-grown VO_2 film. Reconfigurable phase access and hysteresis curve are clearly verified experimentally.

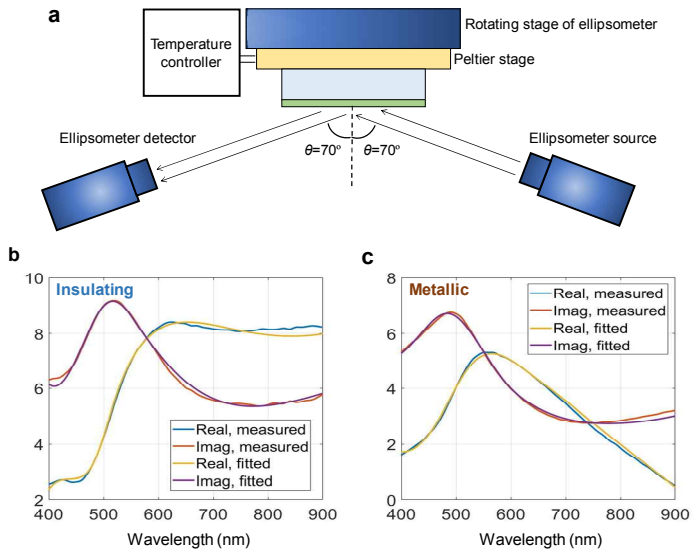

Figure 1.2 (a) Schematic description of ellipsometry with temperature control. (b) Real and (c) imaginary parts of the VO_2 dielectric functions at the insulating and metallic phases from the visible to near-infrared wavelength range. Multiple oscillator fitting data and measured data under Kramers-Kronig relation are compared.

In the context, since the first verification of the IMT by F. J. Morin [22],

extensive studies have been conducted for not only rigorously unveiling the abovementioned physical origin [18, 21] but also novel applications as sensor [23], electronic element [24], and nanophotonic device [25-27]. In particular, the giant electrical resistance tunability induced by the IMT results in large change of the VO_2 dielectric function according to temperature change [18, 28]. Figure 1.2 presents the real and imaginary parts of the dielectric functions in the saturated insulating and metallic phases measured by variable angle spectroscopic ellipsometry. Figure 1.2(a) shows the temperature-controlled ellipsometry scheme in the visible and near-infrared. Temperature control is conducted by Peltier stage (Linkam, PE120) and commercial ellipsometer system (J. A. Woollam, V-VASE) is used.

The multiple oscillator fitting procedure based on previous work is conducted for understanding physical origin of dielectric function spectra [18, 28]. In the insulating phase, dielectric function is fitted to two Tauc-Lorentz oscillators ($\varepsilon_2(E) = \frac{AE_nC(E-E_g)^2}{(E-E_n)^2+C^2E^2}\frac{1}{E}(E>E_g),\ 0\ (E<E_g).$) and the two Lorentz oscillators ($\varepsilon(E) = \frac{AB_rE_n}{E_n^2-E^2-iB_rE}.$).

The fitted parameter sets of the Tauc-Lorentz oscillators are (A, E_n, C, E_g) = (80.104, 5.39392, 11.876, 1.6) and (-31.428, 2.7329, 0.82296, 1.4). The Lorentz oscillators are fitted with parameter sets, (A, E_n, B_r) = (4.8958, 1.158,

0.088137) and (14.381, 2.746, 1.2423).

On the other hand, in the metallic phase, oscillators are set to be the combination of a Drude oscillator ($\varepsilon(E) = \frac{-AB_r}{E^2 + iB_r E}$.), a Tauc-Lorentz oscillator, and a Lorentz oscillator. Parameter sets of the three oscillators are fitted as (A, B_r) = (30.974, 0.43764), (A, E_n, C, E_g) = (137.47, 2.7623, 39.464, 1.9813), and (A, E_n, B_r) = (5.0482, 2.5339, 1.1139), respectively. These modeling results show good agreement with the literature [18, 28] and give good physical intuitions for the two phases.

1.3 Overview of this dissertation

The fundamental research suggested in the dissertation investigates nanoscale interactions between optical range electromagnetic waves and VO_2-included optical gratings for certain application purposes. It is focused on how to design and locate VO_2 nanoantennas, unitcells of gratings, and analyze underlying physics depending on constituent materials and period of gratings. It is shown that reconfigurable thermo-optic modulations of nanoscale near-field and free space far-field are both achieved with the fabricated application devices.

Throughout the dissertation, the proposed research studies have been conducted through three steps in common. At first, theoretical analysis based on plasmonics, Fourier optics, and optical metamaterial is performed using material properties of VO_2 in advance of specific design and demonstration of devices. Secondly, numerical simulations based on finite element method (COMSOL Multiphysics 5.3, RF module) are carried out for design of nanophotonics devices and investigation of the intended tunable photonic performances. Then, nanofabrications with multiple material depositions and definition of nanopatterning using advanced nanoscale focused ion beam (FIB) milling technique are followed for device demonstrations. Lastly,

photonic properties and designed performances of the devices are verified via measurement with properly designed custom-built free space optical systems for imaging and spectroscopy.

The first Chapter is devoted to the introduction of dynamic nanophotonics and material properties of VO_2 in optical range. Context and goals of the field are explained with important tasks and huddles. Then, as a ground work, investigation of VO_2 properties is followed. It is deeply analyzed that optical property change of VO_2 is extraordinary and highly wavelength-dependent.

The main three chapters include the three different themes. Table 1.1 describes summarized contents of the chapters. The second Chapter presents a compact SPP direcitivty switch using asymmetric metagrating idea and VO_2 in the NIR. Momentum of SPP is flipped according to the temperature change in reconfigurable manner.

Table 1.1 Main subjects of each chapter in terms of periodicity of optical grating structures compared to operation wavelength, functions of the devices, bandwidth, and operation regime.

Chapter	**Grating period**	**Functions**	**Bandwidth**	**Operation regime**
2	Near wavelength (subwavelength)	SPP directivity switching	Single wavelength	NIR
3	Larger than wavelength	Transmissivity modulation	Broadband	NIR
4	Deep subwavelength (smaller than half of wavelength)	Color and polarization modulation	Broadband & Narrowband	Visible

In the third chapter, novel method of free space light intensity modulation is proposed. Transmission modulator is demonstrated for high performance operation in the NIR. Without introducing resonant metasurfaces, diffraction grating is designed to be a powerful transmission modulation platform.

The fourth chapter deals with the visible light modulation framework based on VO_2. Reflective deep subwavelength grating, metafilm, is proposed and analyzed thoroughly. The new framework is verified experimentally with applications of large multifunctional color tuning and resonant polarization

conversion.

Chapter 5 will conclude the thesis with the summary and concluding remarks with perspectives.

Chapter 2 Dynamic directional switching of surface plasmon polaritons with metal-VO_2 metagrating

2.1 Introduction

In this chapter, SPPs propagating along the metal-insulator interface is discussed. Hence, it is necessary to start with brief theoretical introduction of SPPs at the simplest single interface geometry with the analytical solution of electromagnetic fields depending only on material properties and wavelength.

Let's consider a two dimensional geometry that a noble metal (ε_m) and a dielectric (ε_d) meet at the interface (z = 0). The Maxwell's equations at the interface yield non-trivial solution of a transverse-magnetic (TM) mode when the sign of the real part of dielectric function in the given geometry is flipped at z = 0. The derived spatial electromagnetic TM field profiles in the area of z > 0 are expressed as [1, 3] :

$$H_y = H_0 e^{jk_{SPP}x} e^{-\kappa_d z}, \tag{2.1}$$

$$E_x = \frac{H_0 j\kappa_d}{\omega\varepsilon_0} e^{jk_{SPP}x} e^{-\kappa_d z},\ E_z = \frac{-H_0 k_{SPP}}{\omega\varepsilon_0} e^{jk_{SPP}x} e^{-\kappa_d z}, \tag{2.2}$$

where ω denotes the angular frequency, ε_0 is the vacuum dielectric function. κ_d and k_{SPP} correspond to the wave vector components along the x-axis and z-axis, respectively. On the other hand, In the area of $z < 0$, similarly,

$$H_y = H_0 e^{jk_{SPP}x} e^{\kappa_m z}, \tag{2.3}$$

$$E_x = \frac{-jH_0\kappa_m}{\omega\varepsilon_0\varepsilon_m} e^{jk_{SPP}x} e^{\kappa_m z}, E_z = \frac{-H_0 k_{SPP}}{\omega\varepsilon_0\varepsilon_m} e^{jk_{SPP}x} e^{\kappa_m z}. \tag{2.4}$$

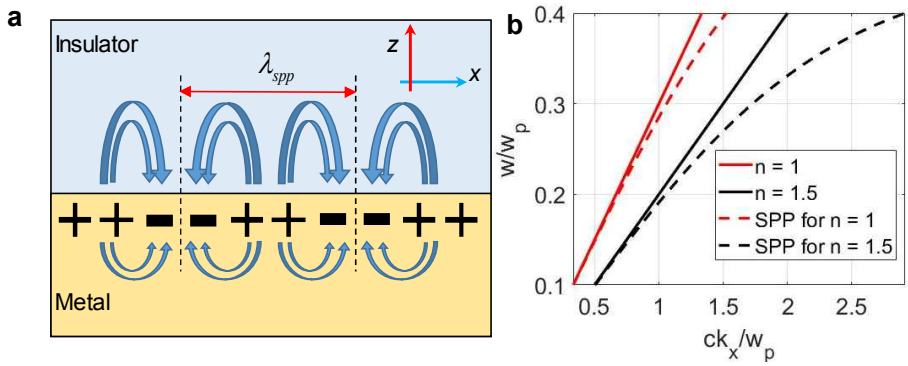

Figure 2.1 (a) Schematic description of electric fields of SPPs at the single interface. (b) Dispersion relations of free space photons and SPPs. ω_p denotes plasma frequency.

The modal characteristic of SPP wave propagation can be explained

clearly by the dispersion relation which originates from the continuity and momentum relation as follows.

$$k_{\mathrm{SPP}} = k_0 \sqrt{\frac{\varepsilon_m \varepsilon_d}{\varepsilon_m + \varepsilon_d}} \,. \tag{2.5}$$

In Figure 2.1(b), the dispersion relations of SPPs are presented using the lossless Drude model metal and non-dispersive insulators. It is clearly shown that SPPs have larger momentum and shorter wavelength than photons in free space at the high energy regime by comparing the dashed line and a solid curve. Thus, to excite SPPs, momentum matching should be introduced for free space photons. Particularly, nanoantennas or nanogratings are preferred for the momentum matching and control of SPPs in the recent plasmonics studies since they can be easily integrated to other devices and have much smaller form factor rather than bulky prism configurations [1, 3, 29-37].

Particularly, in the field of active plasmonics, active reconfigurable switching of near-field directivity with nanophotonic structures, which is an essential functionality for compact integrated photonics and small optoelectronic elements, has been challenging due to small modulation depth

and complicated fabrication methods for devices employing active optical materials [38].

Here, a nanoscale active directional switching of SPPs is demonstrated using the VO_2 phase transition for the first time. The SPP switching device with noticeable distinction is demonstrated based on the phase transition of VO_2 at the telecom wavelength. As the IMT of VO_2 induces the large change of VO_2 dielectric function at telecom wavelengths, the plasmonic response of a nanoantenna made of VO_2 can be largely tuned by external thermal stimuli. The VO_2-insulator-metal (VIM) nanoantenna and its periodic array, the VIM metagrating [35], are suggested as optical switches.

2.2 Principles of metal-VO_2 metagrating

2.2.1 Tunable near-field scattering near VO_2 nanoantenna

The change of dielectric function of VO_2 via the IMT induces the dielectric-plasmonic transition (DPT) phenomenon in the NIR range as shown in Figure 2.2(a). As the real part of dieletric function changes from nondispersive positive value to dispersive negative spectrum, it is optically dielectric in the insulating phase and plasmonic in the metallic phase, respectively. It implies that, in the NIR range, largely switchable subwavelength source can be excited on a VO_2 nanoantenna by light illumination. Furthermore, if a VO_2 nanoantenna is located near a metallic plane, near-field scattering and SPP launching would be induced under TM-polarized illumination. Fig. 2.2(b) describes a scheme of VIM nanoantenna and transmitted SPPs under TM-polarized illumination. Considering high optical loss of VO_2, the deposition thickness is chosen to be 50 nm. Especially, around the telecom band, the real part of the VO_2 dielectric function changes its sign as the phase transition occurs and the difference of the dielectric functions for two phases is fairly large. To effectively utilize large variation of induced dipole moments on the VO_2 slab, a working

wavelength is set to be 1650 nm. Using the measured optical properties, as the ground step, the SPP scattering characteristics of the symmetric VIM nanoantenna buried in the thin metallic plane are analyzed according to the VO_2 phase. A SiO_2 layer of 150 nm thickness is deposited between the 50 nm-thick gold film and the 50 nm-thick VO_2 slab to avoid direct contact between metallic VO_2 and gold. If the VO_2 slab is inserted within the gold film, coupling efficiency of the VIM nanoantenna is reduced significantly when VO_2 is in the metal phase. The thickness of the SiO_2 slab is chosen not to be too thick so that scattering properties of launched backside SPPs are highly affected by the phase of the VO_2 slab, which is located slightly above the gold film.

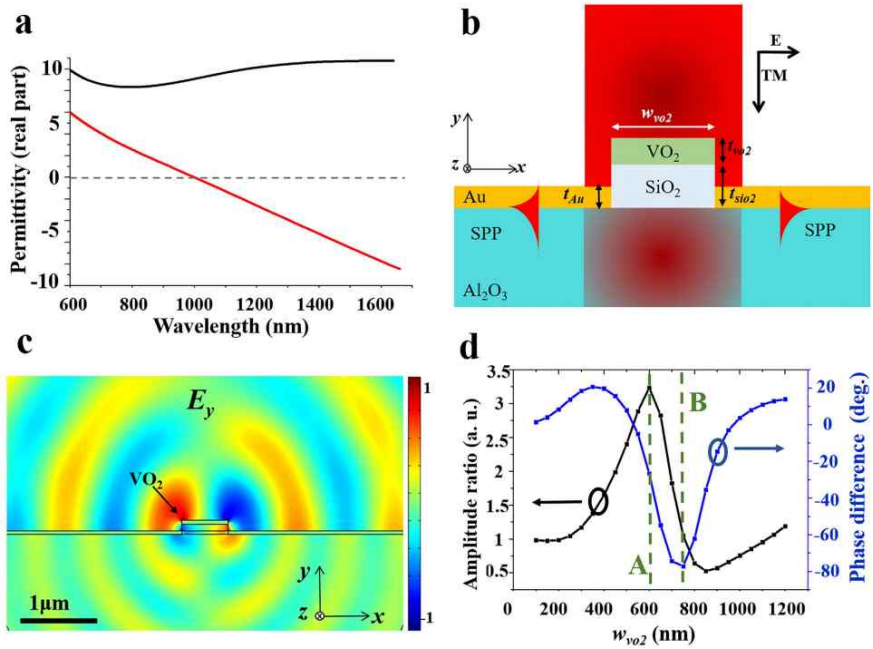

Figure 2.2 (a) Measured near-infrared permittivity (real part) spectra of the VO_2 film at room temperature (the upper black curve) and 90 °C (the lower red curve). (b) A scheme of the symmetric VIM nanoantenna launching SPPs (t_{Au}=50nm, t_{sio2}=150nm, t_{vo2}=50nm). (c) E_y-field profile of the wide symmetric VIM nanoantenna in the insulator phase under incident light of 1650 nm wavelength. (d) IMT-induced amplitude ratio and phase difference between backside SPPs launched in insulator and metal phases according to w_{vo2}.

When the VIM nanoantenna is normally illuminated by a monochromatic laser with TM-polarization as depicted in Figure 2.2(b), two SPP modes with different wavelengths are symmetrically excited on opposite

sides of the gold film which is shown in Fig. 2.2(c). The backside SPP mode is investigated between the two modes in order to separate output signals from the input beam more clearly. The IMT-induced variations of backside SPPs in terms of optical phase and amplitude are highly dependent on the width of the VIM nanoantenna as described in Fig. 2.2(d). In particular, a large amount of variation occurs at two values of antenna width (w_{vo2}), 600 nm and 750 nm, which are marked by dashed lines denoted as A and B in Fig. 2.2(d), respectively. When the VIM width is about 750 nm, phase of the backside SPPs changes by nearly 80° while the amplitude does not change significantly owing to the IMT. It implies that the nanoantenna is suitable for directional switching of SPPs. On the other hand, when w_{vo2} is about 600 nm, the power of the launched SPPs in each phase differs by roughly 10.6 times. Hence, this condition can be useful for on-off switch of backside SPP launching rather than transmissive directional SPP switching. That is, the VIM antenna with the width of around 750 nm is adequate for directional switching of SPPs.

2.2.2 Design of tunable asymmetric launching of surface plasmon polaritons

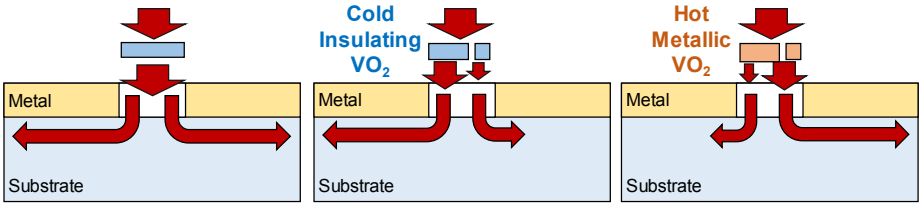

Figure 2.3 Schematic illustration of transmitted SPP generations through (a) symmetric VO_2 nanoantenna and metallic aperture, (b) asymmetric insulating VO_2 nanoantenna and metallic aperture, and (c) asymmetric metallic VO_2 nanoantenna and metallic aperture, respectively, under normal TM illumination.

Based on the analysis of the symmetric case in the previous section, the VIM nanoantenna for asymmetric SPP launching can be designed. Ahead of specific asymmetric VIM nanoantenna design, let us consider the effect of VIM symmetry on the directional backside SPP launching as described in Figures 2.3 (a-c). If asymmetrically shaped double bar VIM is formed slightly above a metallic aperture, large asymmetry of transmitted backside SPPs would be induced and switched by the IMT. Left and right inclined coupling of scattered light with a metallic aperture at the different VO_2 phases would excite left and right inclined directional backside SPPs, respectively.

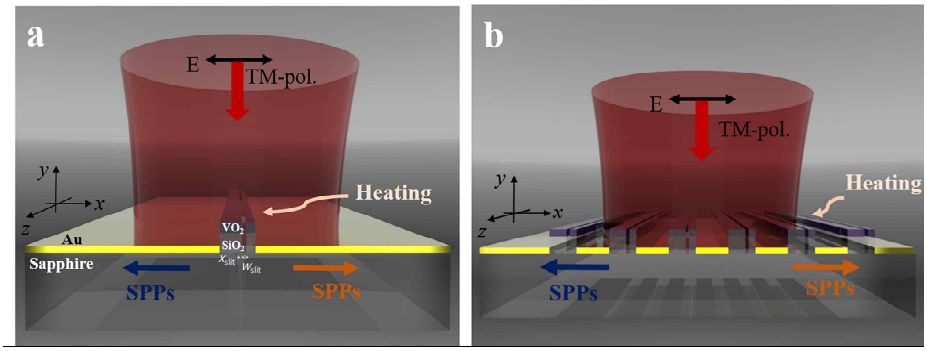

Figure 2.4 Schematic illustrations of (a) asymmetric VIM nanoantenna and (b) subwavelength metagrating made of asymmetric VIM nanoantennas.

The schematic illustration of the asymmetric VIM nanoantenna is described in Fig. 2.4(a). This nanoantenna would be the unitcell of periodically arranged subwavelength metagrating depicted in Figure 2.4(b). A nanoslit in the VIM nanoantenna breaks the symmetry of the structure so that angular distributions of backside SPP scattering patterns show asymmetric directivities. Numerical optimization via parametric sweep of w_{slit} and x_{slit} values while other parameters are fixed. w_{vo2} is fixed as 750 nm. The optimal values of w_{slit} and x_{slit} are 150 nm and 100 nm, respectively, which make distinction ratios of both phases similar [Figures 2.5(a and b)]. Figures 2.5(c and d) graphically verify the balanced asymmetry of SPP launching at the two phases.

As the 0th-order far-field transmission is dominant in case of the

symmetric VIM, asymmetric insertion of the nanoslit into the symmetric VIM can be understood as a small perturbation in the spatial permittivity profile of the VIM structure [Figures 2.5(e and f)]. Hence, it can significantly change the scattering patterns of the backside SPPs while the 0th-order transmission, the main stream of the forward scattering, is not perturbed that much. In Figure 2.5(g), angular spectra of the excited backside SPPs in the insulator and metal phases are depicted when the nanoantenna is optimized by parametric studies. In the insulator phase, the power of the left-directed SPPs is 3.8 times larger than that of the right-directed ones. On the other hand, in the metal phase, the power of the right-directed SPPs is 8.81 times higher than that of the left-directed ones. It is also shown that the forward scattering is not much affected by the IMT of the VIM nanoantenna while backside SPPs are switched as expected [Figures 2.5(e and f)].

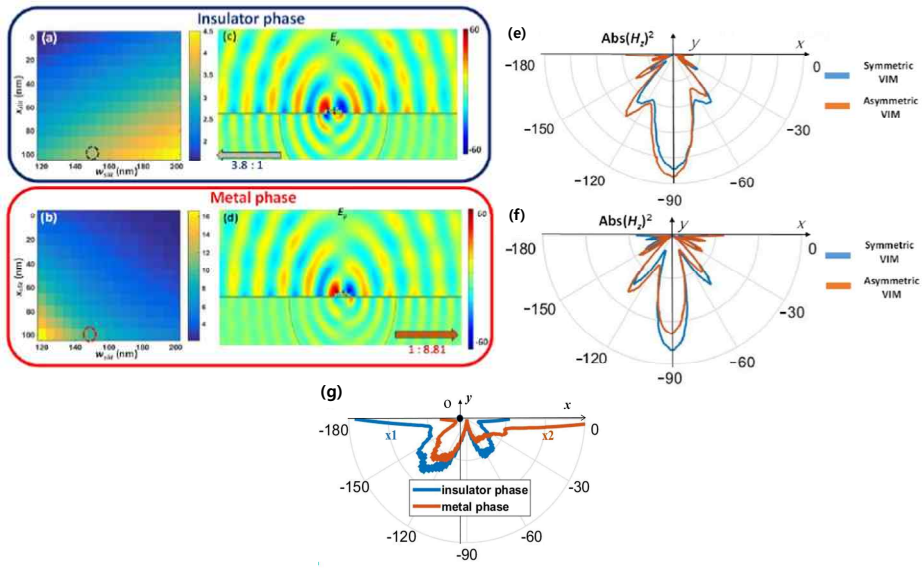

Figure 2.5 (a) Left-to-right power distinction ratio of backside SPPs in the insulator phase according to variations of w_{slit} and x_{slit} (w_{vo2} = 750 nm). (b) Right-to-left power distinction ratio of backside SPPs in the metal phase according to variations of w_{slit} and x_{slit} (w_{vo2} = 750 nm). E_y field profiles in (c) the insulator phase and (d) the metal phase respectively, when the VIM antenna of w_{slit} = 150 nm and x_{slit} = 100 nm is illuminated by the tightly focused Gaussian beam with a waist of 5 μm. Left to right power distinction ratio of backside SPPs in the insulator phase, marked as dotted navy circle in (c), is about 3.8. Right to left power distinction ratio of backside SPPs in the metal phase, marked as dotted red circle in (d), is about 8.81. Spatial distributions of squared magnitudes of transverse magnetic fields which are scattered by symmetric and asymmetric VIM nanoantennas in (e) the insulator and (f) metal phases. Field quantities calculated by simulations are measured along the half circle with a 5 μm radius. The symmetric and asymmetric VIM nanoantennas are located at the center of the half circle. (g) Angular distribution of propagating power carried by backside near-fields in

the both insulator and metal phases.

Although a single asymmetric VIM nanoantenna can be utilized as a directional SPP coupler with thermo-optical switching functionality, SPP coupling efficiency of the single VIM nanoantenna, which is about 0.24 %, is too low to be integrated into plasmonic systems and other applications. Moreover, it is not easy to verify the performance of the nanoantenna experimentally due to its low efficiency. Hence, as mentioned above, a more efficient directional SPP switch named as a VIM metagrating is proposed and demonstrated. As shown in Fig. 4(a), the proposed structure is a periodic array of asymmetric VIM nanoantennas with a period of 932 nm, which is equal to the wavelength of backside SPPs. Each VIM nanoantenna comprising the metagrating exhibits directional SPP launching characteristics in the insulator and metal phases.

$$\Delta k_{x,scatt} = \frac{2\pi}{\lambda_{SPP,back}} m \tag{2.6}$$

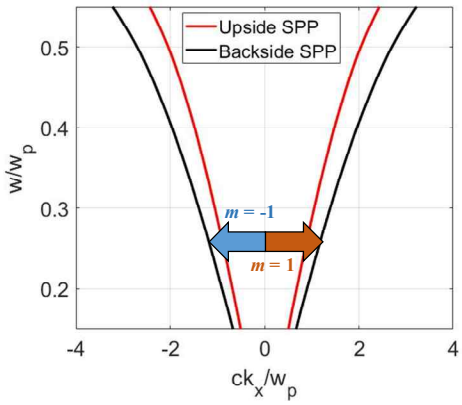

Figure 2.6 Dispersion relations of upside and backside SPPs. The colored left and right arrows describe the grating-induced momentum conservation of backside SPP at the insulating and metallic phases, respectively.

Backside SPPs are basically launched by an additional momentum in the *x*-direction given by the period of the VIM metagrating, as described in Eq. 1. Dispersion relation in Figure 2.6 simply explains the principle of subwavelength grating period can excite switchable backside SPPs rather than upside ones according to the DPT effect. The positive first-order diffraction, denoted as $m = 1$ in Figures 2.6 and 2.7(a), implies right-directed backside SPPs. The negative first-order diffraction, $m = -1$ in Figures 2.6 and 2.7(a), implies left-directed backside SPPs. As a single asymmetric VIM antenna is designed to launch backside SPPs with the distinguished directivities in the insulator and the metal phases, the two first order

diffractions, m = 1 and m = -1, by the VIM metgrating are suppressed in the insulator phase and the metal phase, respectively. Hence, the whole metagrating excites the 0th-order transmission and directional SPPs with opposite directivities in both insulator and metal phases. If directional distinction ratios and switching property of SPP power are preserved in similar levels compared to those of the single asymmetric VIM nanoantenna, higher SPP coupling efficiency can be achieved owing to larger geometric cross-section of the device compared to the single VIM nanoantenna. When w_{vo2}, w_{slit}, x_{slit}, the period, and the number of the periodic VIM nanoantennas are 750 nm, 150 nm, 100 nm, 932 nm, and 7, the ratios of directionally launched SPP power are 8.13:1 and 1:10.56 in the insulator and metal phases, respectively. Figures 2.7(b-e), Ey and Abs(Hz) profiles in both phases, clearly show directional SPP launching characteristics with opposite directivities in both phases.

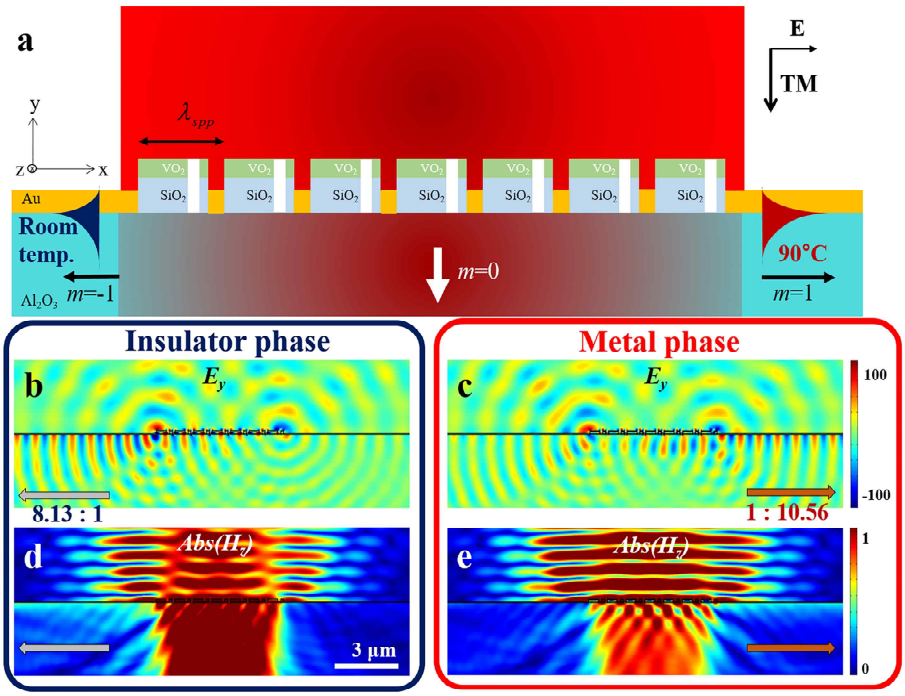

Figure 2.7 (a) Scheme of the VIM metagrating in the metal phase. The proposed VIM metagrating is formed by periodic arrangement of 7 asymmetric VIM nanoantennas with a period of 932 nm. Ey-field profiles in (b) insulator and (c) metal phases, respectively. Magnitude profiles of transverse magnetic fields in (d) insulator and (e) metal phases, respectively. Tightly focused Gaussian beams with a waist of 5 μm are imposed in common for the calculations of (b), (c), (d), and (e). Left to right power distinction ratio of backside SPPs in the insulator phase, as depicted graphically in (b) and (d), is about 8.13. Right to left power distinction ratio of backside SPPs in the metal phase, as depicted graphically in (c) and (e), is about 10.56.

2.3 Experimental demonstration

2.3.1 Fabrication of metal-VO_2 metagrating

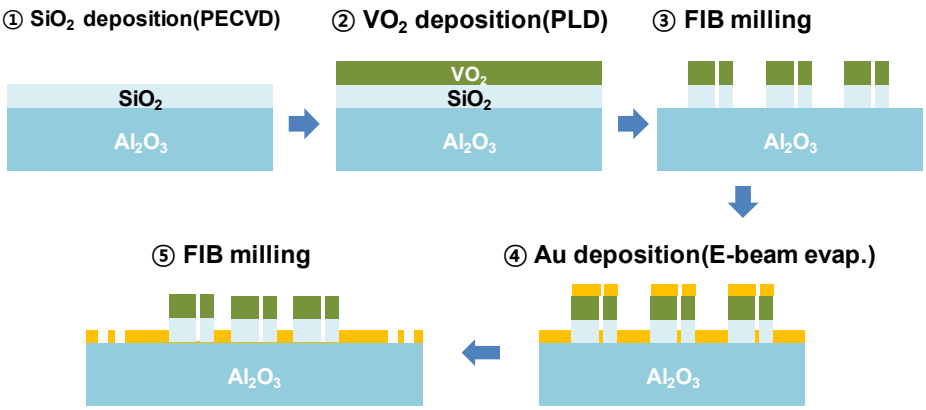

Figure 2.8 Schematic diagram of the 5-step fabrication order for VIM metagrating device exploiting advanced multiple FIB millings.

The device was fabricated by three deposition methods and the two FIB milling processes as described in Figure 2.8. First, a 150 nm-thick SiO_2 layer was deposited on a c-plane sapphire (Al_2O_3) wafer by plasma enhanced chemical vapor deposition (Oxford instruments, PlasmaPro System 100). Pulsed laser deposition (LAMBDA PHYSIK, COMPEX 205) with a KrF excimer laser at 248 nm [21] is utilized for deposition of a 50nm-thick VO_2 film on the SiO_2 layer. In the third step, two large background regions (45 μm by 15 μm) were defined using an FIB milling machine (FEI, Quanta 200

3D) by removing VO_2 and SiO_2 layers except for the VIM metagrating. Then, the periodic arrangement of the 7 asymmetric VIM nanoantennas was defined between those two background regions by utilizing high-resolution milling. Then, the 50 nm-thick gold film was deposited on the VO_2 layer by using an e-beam evaporator (MUHAN, MHS-1800). In the last step, using the FIB machine again, two outcoupler gratings were milled 30 μm far from the metagrating to convert propagating backside SPPs into normally scattered far-fields on both left and right sides of the device. Also, the gold residues deposited on the VO_2 slabs and inside the nanoslits were raked out. As a result, in the middle of two regions with two outcoupler gratings, the VIM metagrating is formed with periodic arrangements of 7 asymmetric VIM nanoantennas with a period of 930 nm. SEM images of the final device are shown in Figures 2.9(a-c).

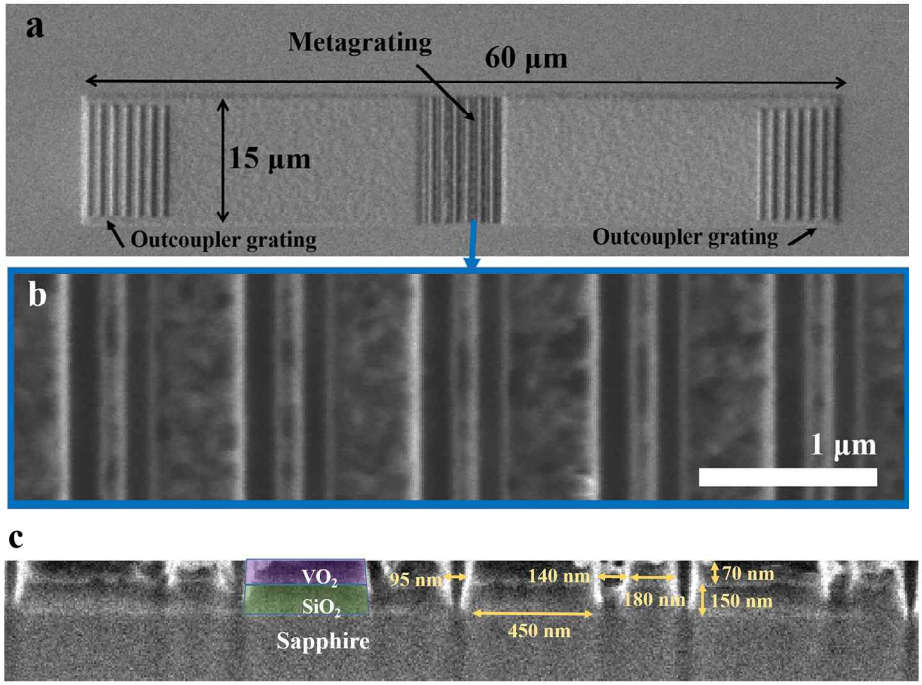

Figure 2.9 (a), (b) SEM topview images of the final device including the VIM metagrating and two outcoupler gratings, and (c) its cross-section image.

2.3.2 Measurement

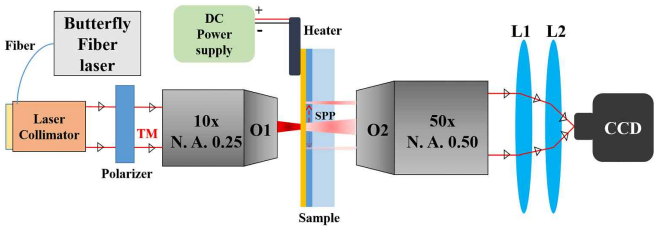

Figure 2.10 Custom-built IR microscopy setup for measurement.

For the last step of experiment, to verify directional launching and switching of SPPs experimentally, a microscopy setup using two outcoupler gratings is built as depicted in Figure 2.10 [35, 39]. A butterfly fiber laser with the wavelength of 1650 nm (Thorlabs, FPL1059S) is collimated and focused on the metagrating sample with a tight beam waist below 20 μm by using an objective lens. When a focused beam illuminates the sample, transmitted backside signals are gathered by another objective lens and imaged by two lenses and an NIR CCD. Firstly, we measure CCD images at the room temperature. Then, the sample is heated over the phase-transition temperature, 90 °C in this case, by using an attached electronic heater and a DC power supply. Finally, the sample is cooled down again to room temperature, and CCD images are measured again to check reconfigurable switching depending on the sample temperature. The temperature of the sample is monitored by using an IR laser thermometer (Testo, 830-T1).

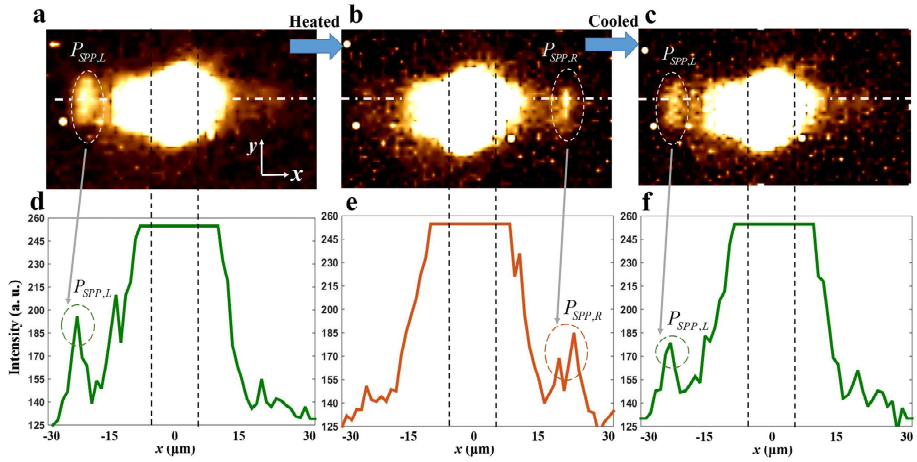

Figure 2.11 IR CCD images when the sample is (a) in the room temperature, (b) heated up to 90 °C, and (c) cooled down to room temperature. (d), (e), (f) Cross-sectional data of far-field intensities according to *x*-coordinate extracted from (a), (b), and (c) respectively. The lines where intensity data are extracted are depicted in (a), (b), and (c) as white dash-dotted lines. The black dashed lines in (a), (b), and (c) indicate position of the sample along the *x*-axis.

When you see Figures 2.11(a and b), the measured NIR CCD images in the insulator phase and the metal phase, clear bright spots at the positions where outcoupler gratings are located are seen at the right and left sides of the metagrating sample, respectively. It means that the IMT of VO_2 induces the directivity switching of asymmetrically launched backside SPPs. Also, when the sample is cooled from 90 °C to the room temperature, as shown in

Figure 2.11(c), position of bright outcoupled signal is reversed back to the position of the left outcoupler grating. Hence, it is verified that the directional launching and switching of SPPs are reversible according to the phase of VO_2 retained in the metagrating. For quantitative analysis of the device performance, the three cross-sectional intensities of transmitted and outcoupled SPP signals along the *x*-direction is plotted in Figures 2.11(d-f). The distinction ratios of overall integrated SPP energies outcoupled from the left and the right gratings are 3.725:1, 1:3.132, and 2.713:1 in those cross-sectional intensity plots, Figures 2.11(d-f). Distinction ratios of SPP powers are calculated considering common intensity offset level, 125, in Figures 2.11(d-f).

2.4 Summary and discussions

In this Chapter, a reconfigurable dynamic switching of SPP directivity via thermally induced IMT of VO_2 is experimentally demonstrated. At first, the VIM nanoantenna is designed as a SPP switching element and then its periodic array, the VIM metagrating, is optimized for higher intensities of coupled SPP signals. In the final step, experimental demonstration of the VIM metagrating verifies that the IMT of a deep subwavelength-sized VO_2-

included nanoantenna is able to switch scattering directions of optical near-fields depending on the temperature. Moreover, it is verified that the switching action is reversible depending on the temperature of the sample. The efficiency of directional SPP launching and switching can be improved if the proposed mechanism is applied to optically resonant nanoantennas or reflection-type configurations rather than transmission type, with more elaborate lithography techniques. By utilizing a resonant and reflective configuration, the number of VIM nanoantenna composing the VIM metagrating can be reduced for smaller footprint of the device. Our demonstration and idea would be meaningful as a proof-of-concept not only to researchers studying plasmonics but also to people developing various active devices for optical beam steering. Furthermore, it also promises potential applications including integrated photonic systems and various reconfigurable imaging systems.

Chapter 3 Broadband efficient modulation of forward transmission with VO_2 diffraction grating

3.1 Introduction

Dynamic modulation of optical transmission intensity is one of the fundamental key technologies in building optical information processing systems for various display, imaging, and communication applications [13, 40]. Owing to large demand on miniaturization and integration of such transmission modulator, various physical principles and devices have been demonstrated for the decades in the field of nanophotonics using reconfigurable optical materials [41-64].

For instance, graphene [41-43] and indium tin oxide (ITO) [44], electrically tunable materials, have been thoroughly studied for modulation of free space transmission in the near-infrared (NIR) and infrared (IR) regime. However, transmission modulators with graphene or ITO have

significant limit in common, ultrathin thickness of active region. Even though graphene shows excellent tunability of dielectric function in the infrared, for large modulation depth and large interaction with light, field-concentrating resonances in metasurfaces should be exploited. Similarly, ITO shows few nanometer-sized ultrathin active regions with tunable dielectric function owing to electron depletion in field-effect based capacitive scheme. Thus, ITO-based field-effect modulators also need nanophotonic resonances in metasurfaces with large electromagnetic field enhancement [44]. It implies that achieving large modulation depth with broad operation bandwidth is limited inevitably when we use graphene or ITO for such transmission modulator. Due to this difficulty, less attention has been paid on it compared to reflective modulator schemes which can take more advantage of strong plasmonic resonances within the ultrathin active regions [45, 46].

On the other hand, PTMs such as VO_2 [18, 28, 49-57], $Ge_2Sb_2Te_5$ (GST) [19, 58-63], and $SmNiO_3$ [20, 64] are advantageous in terms of larger change of dielectric function via application of external thermal, electrical, or optical stimuli. In the NIR and IR regime, Such PTMs prevail ITO and graphene in terms of the degree of modulation of dielectric functions via applied external stimuli. However, despite these advantages of PTMs, efficient, high-contrast, and broadband non-resonant modulation of optical

transmissivity using nanophotonic modulator has not been achieved even with PTMs. Since PTMs are highly absorptive in the NIR and IR, subwavelength-spaced resonant metasurface structure inevitably deteriorate efficiency of transmission unless the thickness of PTM gets extremely thin so that modulation depth of transmission is limited [50, 52-55, 57-61].

Here, a reconfigurable ultracompact transmission modulator working over the broad NIR wavelength region with high efficiency and large modulation depth is proposed and demonstrated. Rather than the conventional resonant metasurface approaches, a novel idea of tunable optical diffraction with high diffraction angle is studied according to the change of the temperature and the corresponding phase of VO_2 over a broad bandwidth. Utilizing the continuous DPT effect of VO_2, at first, we design VO_2 ridge waveguide (VRW) structure for efficient and tunable waveguiding effect for transverse electric (TE) polarization. As the proposed VRW shows largely tunable radiation pattern over broad bandwidth, forward transmission is largely modulated. The key idea is broadband nearly destructive interference between waveguided light and detour light in the insulating phase and suppression of light-VRW interaction in the metallic phase for TE-polarized normal illumination. Via transmission process, incident light is highly diffracted with large deflection angle in the insulating phase, while

normally incident light mainly passes through with little interaction in the metallic phase. Then, the periodically arranged VRWs, phase-transition diffraction grating, is numerically investigated and demonstrated for modulation of the 0^{th} order forward transmission while other oblique diffraction waves with large diffraction angle are considered useless and excluded.

3.2 Principles of VO_2 diffraction grating

3.2.1 Photonic modes in VO_2 waveguide

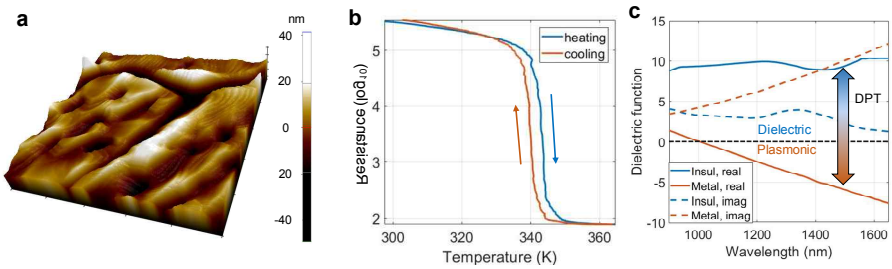

Figure 3.1 (a) 3D atomic force microscopy image of a 340 nm-thick VO_2 film surface. The scanned area is 2 μm by 2 μm. (b) Measured temperature-dependent resistance of a VO_2 film with the hysteric curves of the IMT. (c) Dielectric function spectra at the both insulating and metallic phases in the near-infrared range.

Figure 3.1(a) presents non-contact type atomic force micrograph showing rough surface of a 340 nm-thick VO_2 film fabricated by PLD method. The root mean square surface roughness is about 9.8 nm. Then, the IMT of the thick VO_2 film is verified by measurement of electrical resistance depending on temperature using a source meter, a hot plate, and a thermocouple. As shown in Figure 3.1(b), the conventional electrical characteristic of the IMT is clearly verified.

Then, for optical simulation, dielectric function spectra are investigated

at the insulating (at the room temperature) and saturated metallic (at 383 K) phases, respectively, via spectroscopic ellipsometer (J. A. Woollam, V-VASE) with thermocouple and heater. Figure 3.1(c) presents clearly different complex dielectric functions according to the phase of VO_2 in the NIR. Particularly, real parts of VO_2 dielectric function shows the well-known change from positive to negative value in the wavelength region from 1000 nm to 1650 nm. It implies that in the region, VO_2 shows optical DPT via the thermally-driven IMT. Hence, if TE-polarized light is incident, light can be guided and well-confined inside the insulating VRW structure. On the other hand, in the metallic phase, light cannot penetrate into the VRW structure, thus interaction between light and VO_2 is highly suppressed. In addition, one more noteworthy point is that the dielectric function in the insulating phase is nearly non-dispersive compared to that in the metallic phase.

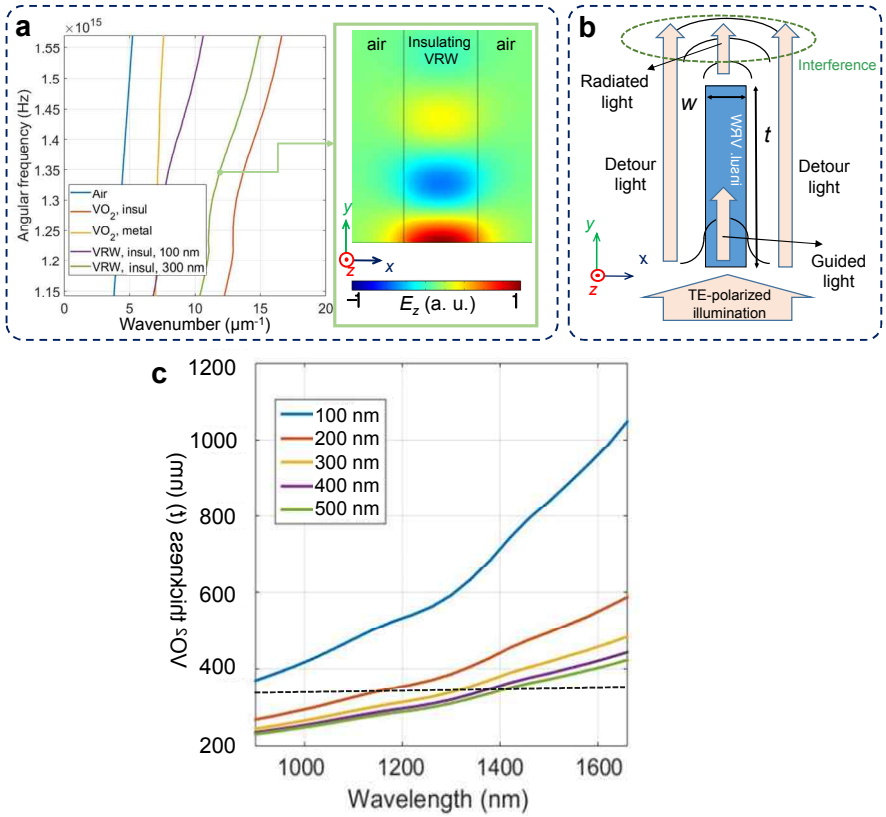

Figure 3.2 (a) Dispersion relations of plane wave in the homogeneous air, the homogeneous insulating VO_2, the homogeneous metallic VO_2, the fundamental TE mode in the 100 nm-wide insulating VRW, and the fundamental TE mode in the 300 nm-wide insulating VRW. The right inset figure depicts normalized E_Z field profile of transverse electric mode guided in the 300 nm-wide insulating VRW at the wavelength of 1400 nm. (b) Schematic image illustrating a VRW and two different types of waves around it (guided light wave and detour light wave) that interfere each other after transmission process. (c) VRW thickness (t) conditions of destructive interference between detour light and guided light in the insulating VRW

over the broad NIR range. The legends denote corresponding width of the insulating VRW. The dashed line denotes t value of 340 nm.

As shown in Figure 3.2(a), the dispersion relations are numerically calculated for understanding TE-polarized light-VRW interaction. The dispersion graph and inset field profile of Figure 3.2(a) implies that the fundamental TE eigenmode guided in the insulating VRW with the width of 300 nm has much larger effective index, gradient of a dispersion curve, compared to that propagating in the air and the mode guided in the 100 nm-wide VRW. High index contrast enables such subwavelength light guiding in the insulating VRW.

Here, we can consider the two types of light waves, detour light and guided light, when TE light is normally incident on the insulating VRW structure as depicted in Figure 3.2(b). While guided light in the 300 nm-wide insulating VRW has the large effective mode index (Figure 3.2(a)), detour light can be considered approximately as plane wave propagating in the air with effective mode index of 1. Thus, inspired by the papers written by M. Khorasaninejad *et al*. involving the designed nanoscale interference around subwavelength dielectric ridge waveguides [65-67], we calculated approximate destructive interference condition for forward diffraction

direction which originates from the effective mode index difference between light that is guided in the insulating VRW and radiated at the end of VRW and detour light. The Eq. (3.1) exhibits the approximate analytical phase matching condition of VRW thickness for forward destructive interference (FDI) [65].

$$t(\lambda, w) \approx \frac{\lambda}{2\{n_{eff}(\lambda, w) - 1\}}. \tag{3.1}$$

In Eq. (3.1), λ and n_{eff} indicate the wavelength and effective mode index of the guided fundamental TE eigenmode, respectively. Figure 3.2(c) presents calculated wavelength-dependent thickness condition of forward-direction destructive interference according to Eq. (3.1) for several widths of VRW. The interesting thing shown in Figure 3.2(c) is that the abovementioned FDI condition does not vary much over the broad NIR wavelength range for wide VRWs (width of 300-500 nm). As marked as the black dashed line in Figure 3.2(c), if the t of insulating 300 nm-wide VRW is set to be 340 nm, FDI condition is approximately met for broad wavelength range around the wavelength of 1400 nm. It means that broadband suppression of forward diffraction with nearly destructive interference is achieved around the wavelength of 1400 nm if the amplitude of detour light and that of light radiated from the end of the insulating VRW are balanced.

Moreover, it has been shown that large angle (above 30°) beam diffraction is achieved when the FDI condition is met in the previous studies involving DRWs by M. Khorasaninejad *et al*. [65-67]. Thus, we can expect such large angle diffraction around the wavelength of 1400 nm via amplitude balancing optimization.

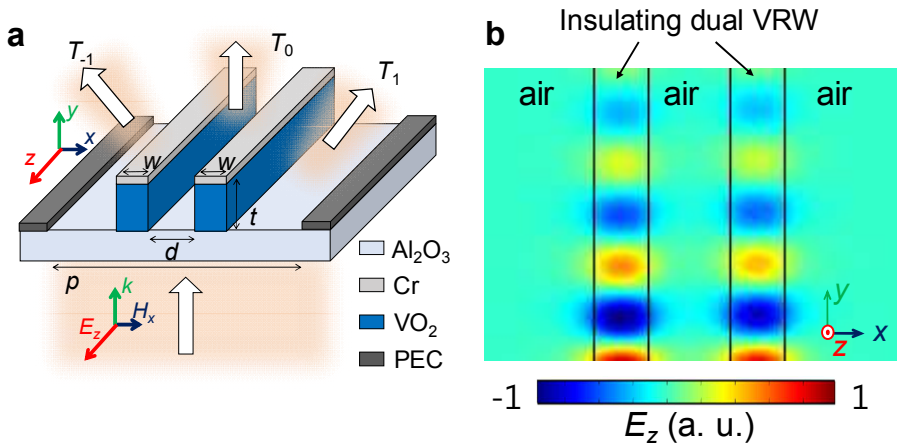

Figure 3.3 (a) Schematic illustration of dual VRW for TE-polarized normal illumination. *w*, *t*, *d*, and *p* quantities are 300 nm, 340 nm, 450 nm, and 2200 nm, respectively. (b) Spatial E_z field distribution of the numerically solved fundamental TE eigenmode of the dual VRW described whose *w* and *d* values are 300 nm and 450 nm, respectively. The guided eigenmode is calculated at the wavelength of 1400 nm.

However, ahead of the unitcell VRW design, we should design diffraction grating period (the total *x*-directional width of the unitcell) large

enough to bend the first diffraction order with the angle around 30 °, the width of the VRW unitcell. Thus, grating period is set to be 2.2 μm so that the diffraction angle ($\sin^{-1}(\lambda/p)$) in the wavelength region of interest (1000-1650 nm) ranges from about 27 ° (at 1000 nm) to 49 ° (at 1650 nm). Due to the large grating period, however, it is hard to balance amount of detour light and guided light with single 300 nm-wide VRW since most amount of incident light becomes detour light [65]. Hence, we located two identical 300 nm-wide VRWs with separation distance (d) of 450 nm for the optimization of the balancing as described in Figure 3.3(a). Figure 3.3(b) depicts the guided fundamental TE eigenmode in the dual VRW whose w and d values are 300 nm and 450 nm, respectively. It is graphically shown that negligible coupling occurs between the two distinct VRWs owing to subwavelength confinement. The 10 nm-thick Cr is located on the VRWs considering improved tapering issue and preventing Ga+ ion contamination during ion beam milling process. In the simulation configuration, the two 10 nm-thick perfect electric conductor plates are located to set the incident beam size to be 2.2 μm while plane wave with TE polarization is incident from the substrate side.

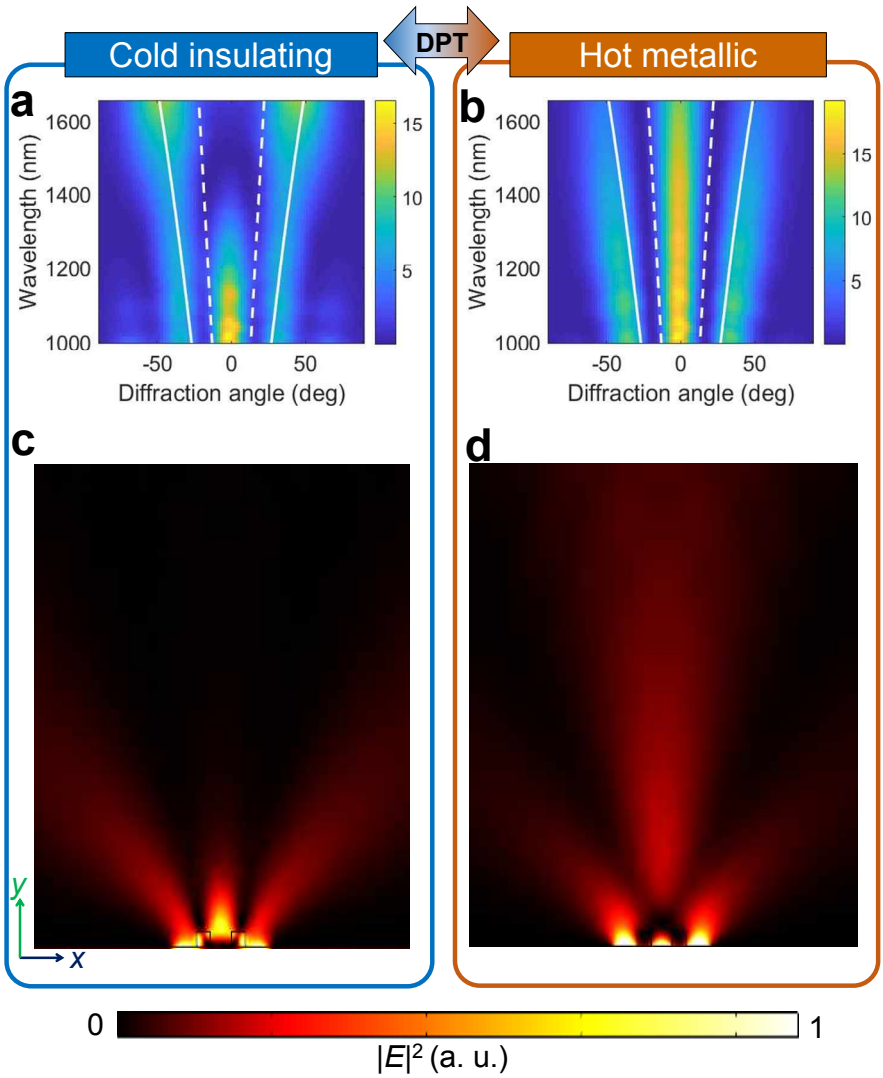

Figure 3.4 Transmissivity plot of the dual VRW unitcell described in Figure 3.3 according to radiation angle and wavelength at (a) the insulating and (b) metallic phases, respectively. The white and white dotted lines in (a and b) denote theoretical constructive and destructive diffraction conditions of the grating with period of 2.2 μm, respectively. Normalized transmitted electric field intensity distributions at (c) the insulating and (d) metallic phases,

respectively. The wavelength is set to be 1500 nm in common.

The largely tunable diffraction directivity of the dual VRW unitcell is investigated for the broadband wavelength range [Figures 3.4(a and b)]. Figure 3.4(a) show that the forward transmission is suppressed for broad bandwidth at the insulating phase. Especially, FDI occurs clearly at the wavelength range from 1400 to 1600 nm while moderate suppression of forward transmission occurs at the wavelengths of 1100 and 1400 nm. On the other hand, at the metallic phase, owing to the DPT phenomenon, interaction between TE-polarized light and the dual VRW decreases dramatically over broad bandwidth. Hence, most of light transmission is heading forward at the metallic phase [Figure 3.4(b)]. Figures 3.4(c and d) exhibit graphical verification of such high contrast change of forward transmitted diffraction via the DPT while oblique sidelobes do not change largely.

The interesting point is that theoretical destructive and constructive diffraction conditions of the dual VRW unitcell nearly correspond to diffraction simulation results of the dual VRW unitcell regardless of the VO_2 phase. The theoretical destructive ($p\sin\theta = \lambda/2$) and constructive ($p\sin\theta = \lambda$) conditions of diffraction grating are marked as the white and white dotted lines in Figures 3.4 (a and b), respectively. In other words, if the unitcell is

periodically arranged as a diffractive grating with the period of p (2.2 μm), the -1st and 1st diffraction orders of the grating would be deflected with the angle nearly similar to the angles of the oblique diffraction by the unitcell.

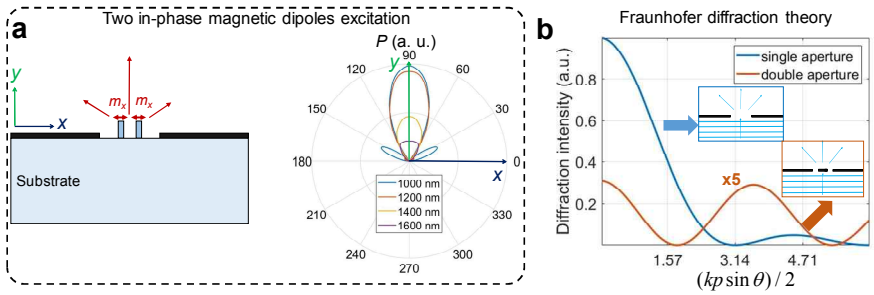

Figure 3.5 (a) Scheme of the dual VRW unitcell excited by the two horizontal magnetic dipoles light above the end facets of two VRW structures (left figure). The right figure of angular power spectrum shows nearly forward scattering of the unitcell induced by the corresponding excitation. (b) Theoretical calculation results of the single and double aperture Fraunhofer diffraction intensities with the similarly located minimums and maximums. The inset figures denote the two Fraunhofer diffraction configurations. The double aperture is constructed by symmetrically blocking the central part of the single aperture by 3p/4 (1.65 μm) wide perfect electric conductor plates between them described in Figure 3.5 (a) and 3.3 (a). The whole width of single and double apertures is same with the unitcell width, 2.2 μm.

The abovementioned similarity between the diffraction directivity of the unitcell and that of the periodically arranged grating can be explained by

investigation of the two different light-VRW interaction channels. When TE polarized light illuminates the dual VRW structure, light is transmitted by detour or waveguiding as described above. Thus, diffraction pattern is generated by the detoured aperture diffraction effect and re-radiation of horizontal magnetic dipolar radiation at the end facets of VRWs. The schematic image of Figure 3.5 (a) describes effect of the two in-phase magnetic dipoles excited at the end facets of two VRWs. The right polar plot of Figure 3.5 (a) shows that nearly forward diffraction occurs dominantly. It means that re-radiated light from the VRWs do not contribute to oblique sidelobes. On the other hand, transmitted light which detours the dual VRW and 2.2 um-wide aperture is diffracted mainly into the three directions in the wavelength range of 1000-1650 nm. Figure 3.5 (b) shows the analytically derived Fraunhofer intensity patterns for the single and double apertures depicted in the inset pictures. The single aperture diffraction pattern deviates from the diffraction orders largely since the 1st minimum of single aperture correspond to the 1st diffraction order of grating. However, the double aperture scheme which consider VRW detour effect shows the more reasonable diffraction pattern accountable for the dual VRW radiation pattern. The double aperture scheme is constructed by adding a perfect electric conductor plates at the center of the single aperture scheme by considering

effective scattering cross-section of the dual VRW structure. As a result, the position of 1st minimum and 1st maximum would decrease toward $kp\sin\theta/2$ is about $\pi/2$ and π, respectively. It implies that the proposed double aperture Fraunhofer diffraction modeling is clearly accountable for VRW detour effect and aperture diffraction simultaneously.

3.2.2 Design of VO_2 grating modulator

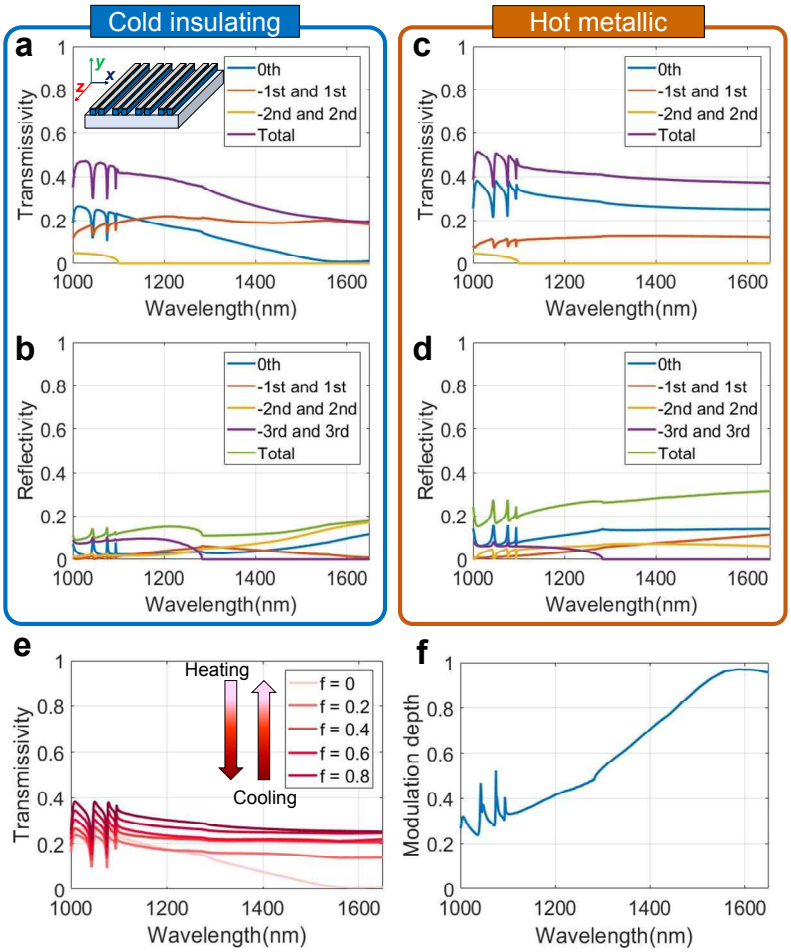

Figure 3.6 (a) Transmissivity and (b) reflectivity spectra of the diffraction grating modulator in the insulating phase. The inset picture describes the scheme of the dual VRW based diffraction grating (period = 2.2 μm). (c) Transmissivity and (d) reflectivity spectra of the diffraction grating modulator in the metallic phase. The legends describe the corresponding diffraction orders. (e) Simulation results of the 0^{th} order transmissivity

depending on the filling factor (f) of the metallic VO_2 during continuous phase transition. The legends denote to corresponding filling factor of the metallic VO_2. Here, $f = 0$ and $f = 1$ imply the insulating and metallic phases, respectively. The intermediate f values between them correspond to the intermediate temperatures of the mixed phases where the two distinct phases coexist. (f) Numerically calculated modulation depth (η_m) spectrum.

The VRW grating described in the inset image of Figure 3.6(a) is composed by periodic arrangement of the optimized dual VRW unitcell which consist of 2.2 μm-wide aperture and the dual VRW. As mentioned above, the grating period is equal to the unitcell width (2.2 μm). Since the unitcell is designed to suppress forward transmission not in the metallic phase but in the insulating phase, transmissivity in the metallic phase is shown to be much higher over the broad bandwidth in non-resonant manner [Figures 3.6(a and b)]. Reflectivity is relatively weak over the broad NIR bandwidth regardless of diffraction orders and phase of VO_2 while transmissivity is relatively large due to large grating period and small VRW sizes [Figures 3.6(a-d)].

The reconfigurable VRW grating modulator can continuously modulate transmission signal according to continuous change of the sample temperature. Thus, for numerical estimation of the continuous modulation capability utilizing intermediate phases where the insulating and metallic

phases coexist, we also investigate the 0^{th} order transmissivity at the intermediate phases according to filling factor (*f*) of the metallic phase by help of Maxwell-Garnett effective medium theory (EMT) [6]. When *f* varies from 0 to 0.4, host material is set to be the insulating VO_2 ($\varepsilon_{eff}(f) = \varepsilon_i \{\varepsilon_m(1+2f) + \varepsilon_i(2-2f)\} / \{\varepsilon_m(1-f) + \varepsilon_i(2+f)\}$). On the other hand, when *f* varies from 0.6 to 1, host material is set to be the metallic VO_2 ($\varepsilon_{eff}(f) = \varepsilon_m \{\varepsilon_m \cdot 2f + \varepsilon_i(3-2f)\} / \{\varepsilon_m(3-f) + \varepsilon_i \cdot f\}$). By using such *f*-dependent dielectric functions of intermediate phases with EMT, the continuously modulated 0^{th} order transmissivity is numerically calculated and presented in Figure 3.6(e). Resultantly, as shown in Figure 3.6(f), the large modulation depth from about 0.35 to 1 is achieved in the 1100 nm – 1650 nm wavelength region. Modulation depth of transmissivity, η_m, is defined as $\eta_m = |T_i - T_m| / \max(T_i, T_m)$ where T_i and T_m denote the 0^{th} order transmissivities in the insulating and metallic phases, respectively.

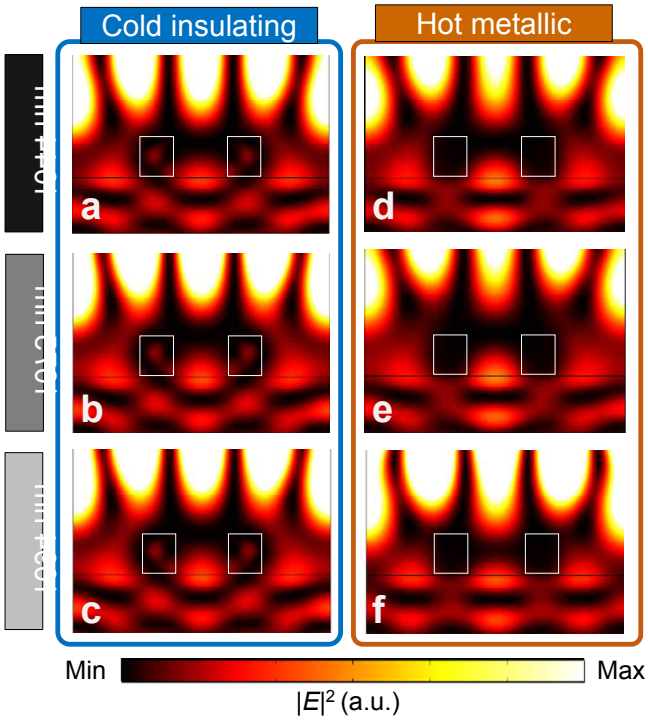

Figure 3.7 Spatial distributions of electric field intensity near the grating structure at the three leaky mode resonances at the (a-c) insulating and (d-f) metallic phases. The resonance wavelength is (a and d) 1044 nm, (b and e) 1075 nm, (c and f) 1094 nm.

The three sharp resonances at the both phases in the short wavelength region of 1000-1100 nm are leaky mode resonances [Figure 3.6]. These resonances facilitate absorption by resonantly localizing leaky waves between the VRW structures rather than in them [Figure 3.7]. Thus, leaky wave interaction with the VRW structure is enhanced at the both phases of

VO_2. As electric field is mainly confined between the VRW structures, not the locations of resonance wavelengths but the resonance strengths are affected by phase transition of VO_2.

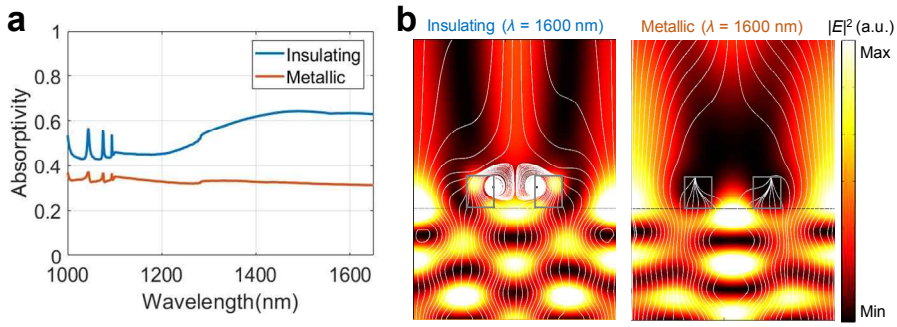

Figure 3.8 (a) Broadband absorptivity spectra of the VRW grating modulator. (b) Spatial distributions of electric field intensity and stream line of Poynting vector near the grating structure at the insulating (right) and metallic (left) phases, respectively. The wavelength is 1600 nm in common.

Change of power dissipation and flow is investigated for in-depth physical analysis of the transmission modulator. Absorptivity spectra in Figure 3.8(a) shows that absorptivity is enlarged in the insulating phase compared to the metallic phase over the broad NIR bandwidth. It is owing to enhancement of waveguiding and relieved detour effect as shown in Figure 3.8(b). At the wavelength of 1600 nm where FDI condition is accurately

achieved, field confinement is enhanced and suppressed in the insulating and metallic phases, respectively. Figure 3.8(b) describes such phenomena with the change of Poynting vector flow marked as white stream lines. In the insulating phase, considerable amount of stream lines is inhaled by the VRWs. On the other hand, in the metallic phase, most of power stream detours them.

3.3 Experimental demonstration

3.3.1 Fabrication of VO_2 grating modulator

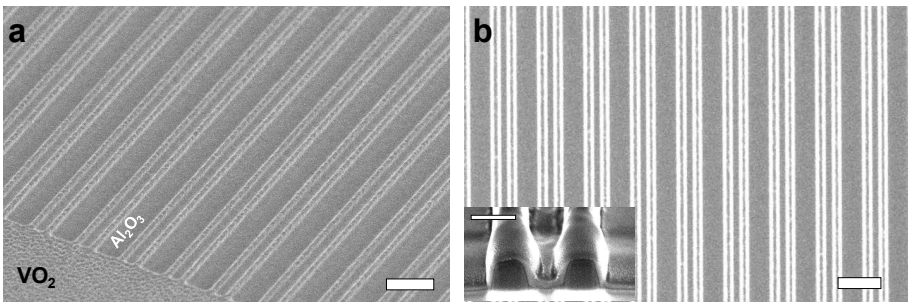

Figure 3.9 Scanning electron micrographs of the fabricated VRW grating of (a) oblique and (b) top views. The inset image of (b) shows cross-sectional view of the VRW grating. The scale bars denote 2000 nm, 500 nm, and 2000 nm, from the left to right, respectively.

For experimental verification, the VRW grating transmission modulator sample is fabricated via three processes. At first, a 340 nm-thick VO_2 film is deposited via conventional PLD method. Then, 10 nm-thick Cr protection hard mask is deposited via e-beam evaporation (Korea Vacuum Tech, KVE-3004) on a VO_2 film. The thin Cr hard mask plays a role to reduce tapering effect of ion beam milling and reduce stoichiometric effect of Ga^+ ion on VO_2 [68]. At last, 110 μm by 110 μm sample is defined by multiple processes

of focused ion beam milling with translational movements (FEI, Quanta 200 3D). Figures 3.9(a and b) shows the scanning electron micrographs of the fabricated VRW grating modulator.

3.3.2 Measurement

The 0^{th} order transmission spectrum is measured with a custom-built free space near-infrared spectroscopy setup described in Figure 3.10(a). The super-continuum light source (NKT Photonics, Super EXTREME EXR 15) is tightly focused with objective lens on the sample as a broadband source. Then, only forward transmission signal is collected by objective lens with whose NA is 0.45. As the minimum first-order diffraction angle is about 27 ° and the corresponding NA value is about 0.5 at the wavelength of 1000 nm, filtering of the oblique diffraction waves is achieved over the broad measurement bandwidth (1000-1650 nm). The signal is collected by an optical fiber and decomposed by optical spectrum analyzer (YOKOGAWA, AQ6370D). Figures 3.10 (b and c) correspond to measured transmission spectra while heating and cooling processes. Figure 3.10 (d) shows the linear curve fitting results of the transmissivity for analyzing broadband overall trend of spectrum variation at the insulating and metallic phases. Figure 3.10

(e) suggests the measured and linearly fitted modulation depth spectra implying broadband high contrast modulation performances. It is verified that the efficient, broadband, and high-contrast modulation performance of fabricated sample shows similar modulation trend with numerical simulation results in Figure 3.6(c).

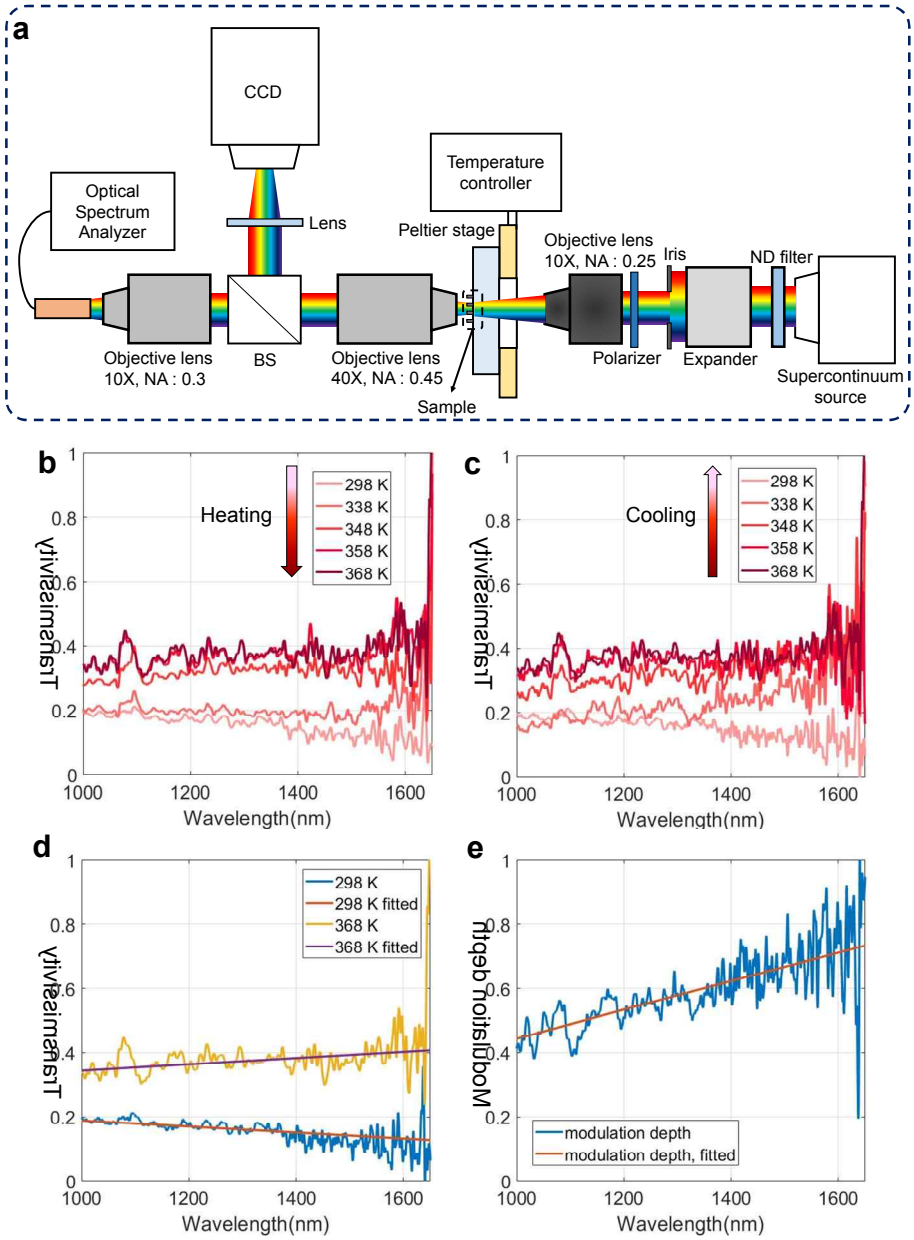

Figure 3.10 Figure 3.10 (a) Custom-built temperature-controlled micro-spectroscopy setup scheme for the 0^{th} order transmission measurement. The measured 0^{th} order transmissivity spectra in (b) heating and (c) cooling

processes, respectively. (d) Linear curve fitting analysis of the measured 0^{th} order transmissivity. The legends describe measured data and fitted linear line at the insulating and metallic phases. (e) Measured modulation depth and linearly fitted line.

The large noise of measured spectra in the long wavelength range is due to bandwidth restriction of the optic components (1000-1600 nm) and optical spectrum analyzer (800-1700 nm) and significant power reduction by input beam filtering parts with an iris, a beam expander, and a ND filter. Thus, power spectrum of input source is significantly lowered specifically in the long wavelength region near 1500-1650 nm.

3.4 Summary and discussions

In this Chapter, a novel reconfigurable nanophotonic solution for ultracompact, broadband, high efficiency, and high contrast modulation of optical transmission is proposed and demonstrated. The proposed phase-transition VRW grating acts as a high performance transmission modulator based on waveguiding of TE-polarized light, optical DPT phenomenon of VO2, and proper grating period which is larger than the wavelength. The operation bandwidth of 450 nm is verified with nearly non-resonant on-state transmissivity about 0.4 and minimum modulation depth about 0.4. The fast electrical modulation of phase transition would be also possible when the metallic thin film micro-heater is integrated to the device [50, 69]. Furthermore, the proposed scheme is also applicable to other PTMs such as GST which exhibits similar DPT effect in optical range [59]. It is expected that the proposed idea and device would be fruitful for various broadband optical modulators and building novel high resolution ultracompact spatial light modulators in the NIR and IR regime.

Chapter 4 Tunable multifunctional phase-transition effect with noble metal-VO_2 metafilm in the visible

4.1 Introduction

Here, a fundamental study on phase-transition metafilm via combination of noble metal (Ag) inclusions and VO_2 is proposed to improve such intrinsic limits of the material in the visible spectrum inspired by metamaterial theory. Based on mirror-enhanced near-unity absorption and effects of deep subwavelength noble metal inclusions, designing effective refractive indices of a phase-transition layer is demonstrated within reflective phase-transition metafilms. Utilizing large anisotropy of the inclusions, it is verified that the metafilm strategy increase dynamic shifts of absorption dip wavelength nearly two times from about 70 nm to about 140 nm while wide dynamic coloring and polarization tuning are achieved in the visible. The concepts suggest the fundamental solutions to ameliorate limited functionality, extensibility, and modulation contrast in the phase-transition nanophotonics

in the visible range.

4.2 Absorbing Ag-VO_2 metafilm in the visible

4.2.1 Role of metallic mirror

As the ground work, firstly, we begin with investigation of tunable optical properties of a bare 40 nm-thick VO_2 film via the reconfigurable continuous IMT phenomenon. Figure 4.1(a) describes measured thermally-driven reconfigurable evolutions of complex refractive index coordinates, (*n*, *k*), at the four representative wavelengths (blue: 473 nm, green : 532 nm, red : 633 nm, and deep red : 700 nm). n and k denote real and imaginary parts of complex refractive index of VO_2, respectively. Interestingly, increase of temperature leads to continuously decreasing tendencies of both *n* and *k* values regardless of wavelength while they show simultaneously large values. Thus, we would call this phenomenon 'the high refractive index to low refractive index transition (HLT)' rather than the IMT throughout the manuscript. The continuous HLTs between the saturated insulating and metallic phases depend on the intermediate temperatures during heating and cooling processes. It implies that heating and cooling would induce gradual blue and red shifts of resonances in a VO_2-included nanophotonic resonators.

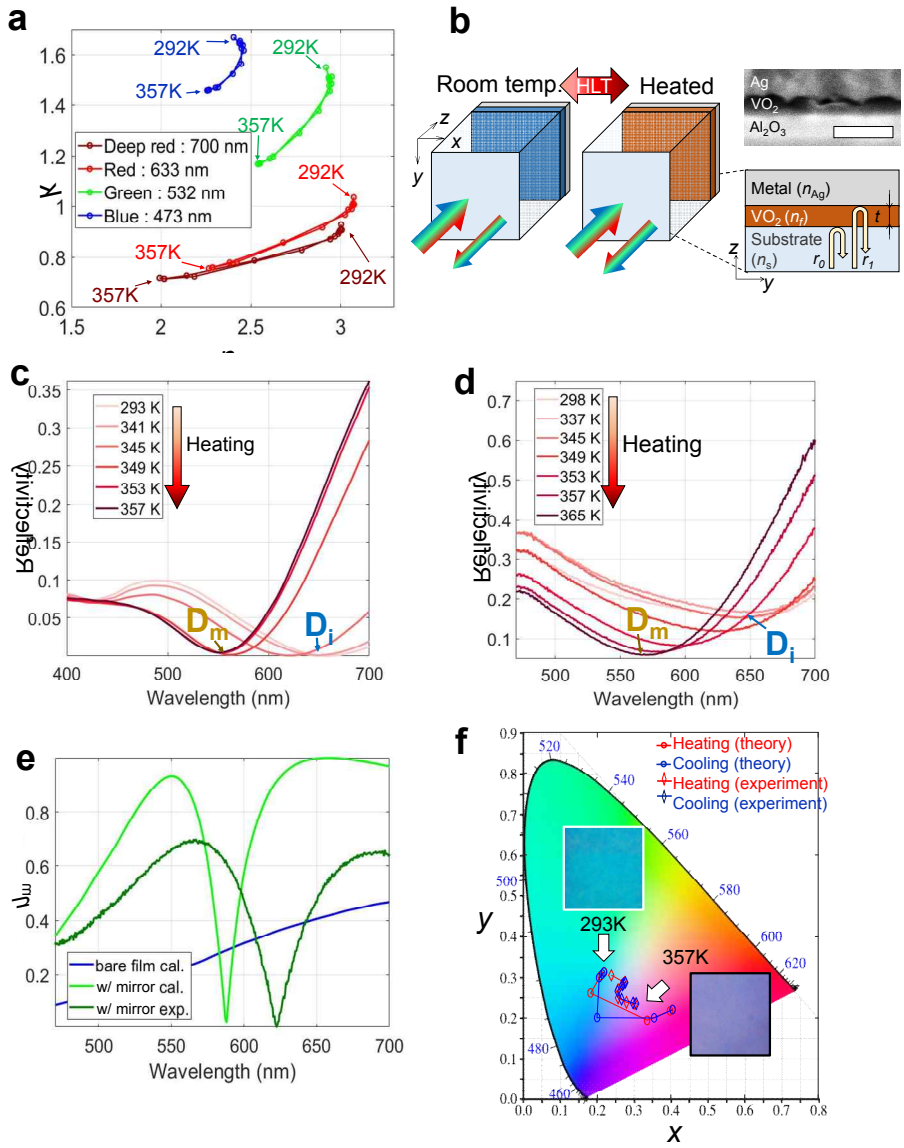

Figure 4.1 Role of noble metallic mirror for an enhanced phase-transition thin film. (a) Measured thermally driven cyclic evolutions of (n, k) coordinates of VO_2 at the representative blue (473 nm), green (532 nm), red (633 nm), and deep red (700 nm) colors. (b) Schematic illustration and cross-

sectional SEM image of the sapphire substrate-40 nm-thick VO_2-Ag mirror multilayer structure. Scale bar in SEM image denotes 100 nm. Heating induced multi-level modulation of near-unity absorption in (c) theoretical calculations and (d) measurements. (e) Modulation depth spectra of the 40 nm-thick bare VO_2 film and the silver mirror-coated VO_2 film in the visible spectrum. (f) Heating and cooling induced multi-level color generations by the mirror-coated VO_2 film described in a CIE space.

However, a bare VO_2 film is intrinsically limited to low modulation performance owing to theoretically limited maximal absorption of 0.5 [71, 72]. For large modulation depth (η_m) of light intensity, near-unity absorption is essentially required as it enables near-unity quantity of η_m. ($\eta_m = |I_i - I_m| / \max(I_i, I_m)$) I_i and I_m correspond to reflection intensities at the insulating and metallic phases, respectively. η_m is a quantity between 0 and 1. Thus, for enhancing visible light intensity modulation, we introduce the LTFI mechanism to design metallic mirror-assisted near-unity absorptions in a VO_2 thin film. Figure 4.1 (b) shows the scheme and cross-sectional SEM image of the VO_2 thin film on the Ag mirror where the both sides of the 40nm-thick VO_2 film are capped by a sapphire substrate and a Ag mirror. As shown in Figures 4.1(c and d), the two distinct near-unity absorptions in the insulating and metallic phases at the wavelengths of 655

nm and 550 nm are verified through the theoretical calculation and measurement. As expected from the HLT phenomenon, heating and cooling induce the continuous blue and red shifts of absorption dip with about 100 nm change in the resonance wavelength, respectively (See Figures 4.1 (c and d).).

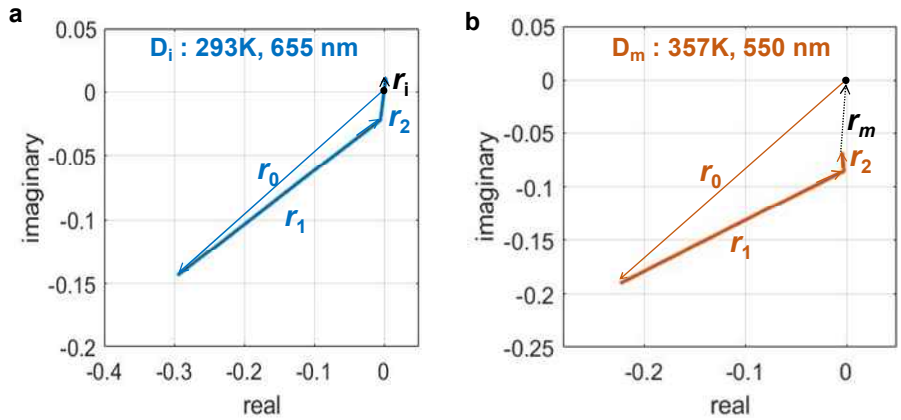

Figure 4.2 Complex plane describing destructive interferences of dominant partial reflection phasors at the near-unity absorption dips of sapphire-40nm thick VO_2 film-Ag mirror multilayer structure. The interferences of the dominant three lo1west order phasors at (a) room temperature and wavelength of 655 nm and (b) 357 K and wavelength of 550 nm, respectively.

Physical origins of such dips can be explained by the theory of LTFI. It is known that a near-unity absorption based on LTFI is dominantly determined by the two lowest orders of partial reflection phasors, r_0 and r_1

[72, 73]. Here, $r_0 = (n_f-n_s)/(n_s+n_f)$ and $r_1 = t_1t_2r_m\exp(2jn_fk_0t)$ when $t_1 = 2n_s/(n_s+n_f)$, $t_2 = 2n_f/(n_s+n_f)$, and $r_m = (n_{Ag}-n_f)/(n_{Ag}+n_f)$ (n_f, n_s, n_{Ag}, k_0, and t denote complex refractive indices of a VO_2 film, substrate, a Ag mirror, free-space wavenumber, and thickness of a VO_2 film, respectively.). Higher order partial reflection phasors, $r_n = t_1t_2r_m^n(-r_0)^{n-1}\exp(2jn_fk_0t)$ for $n>1$, are negligible owing to small amplitudes resulted from multiple scatterings in destructive interference (See Figure 4.2.).

Through large blue and red shifts of near-unity absorption in the phase-transition VO_2 film on the mirror, performances of modulation depth and color tunability are strongly enhanced compared to a bare VO_2 film. Figure 4.1(e) reveals that phase-transition film on mirror shows broadband enhancement of except the wavelength region near the dips of (wavelengths about 590 nm and 620 nm in the calculation and measurement results, respectively.), where reflectivity spectrum curves at the insulating and metallic phases cross each other [Figures 4.1(c and d)]. In case of color generation, as shown in Figure 4.1(f), the continuous reversible color change between sky blue and purple inclining to red is verified both in calculation and experiment. The circles and diamonds in CIE diagram correspond to CIE coordinates at the different temperatures during heating and cooling processes shown in Figures 4.1(c and d) and Figure 4.3. Compared to a bare

VO_2 film case which shows very small shift of CIE coordinate around near-white color, it is obvious that the color tunability is highly enhanced.

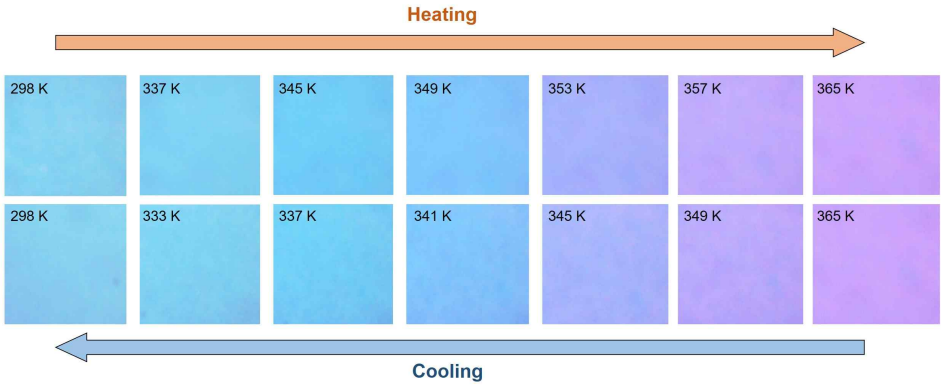

Figure 4.3 Dynamic multi-level coloring through heating and cooling in the 40 nm-thick VO_2 film capped by the Ag mirror and the Al_2O_3 substrate.

4.2.2 Role of effective medium approximation for dynamic metafilm

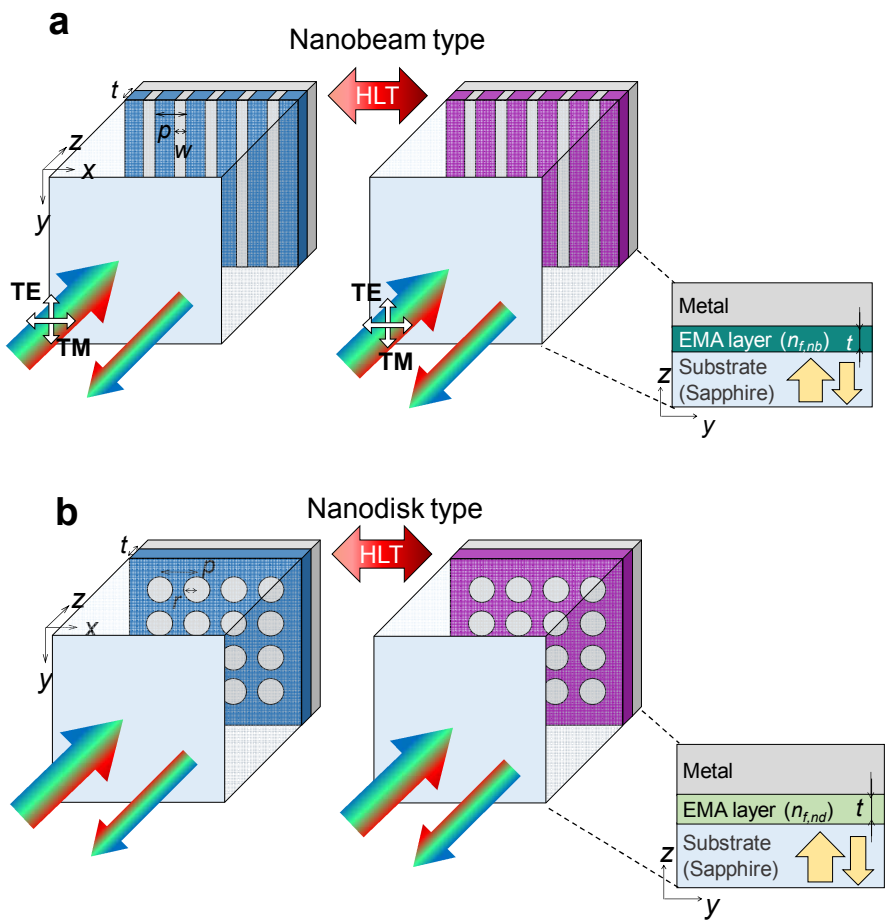

Figure 4.4 Schematic illustrations of reflective (a) nanobeam (NB)-type and (b) nanodisk (ND)-type metafilms with the HLT driven blue shifts of absorption dips, respectively. Cross-sectional scheme shows that periodically implanted metallic inclusions in a VO_2 film with 200 nm period can be approximately modeled as effective medium layer with tunable ECRIs.

Even if the phase-transition VO_2 film on metallic mirror shows the strongly enhanced tunability of broadband intensity and color in the visible, design degree of freedom of locating near-unity absorption dip and designated functionality are still limited. Intuitively, we can expect that increase and decrease of VO_2 film thickness would induce red and blue shifts of near-unity absorptions. However, it is not easy to design by only adjusting thickness of VO_2 film to meet complex matching conditions of amplitude and phase of reflection phasors.

Here, we introduce a metamaterial-based fundamental solution to expand range of possible ECRI of PTM layer by implanting subwavelength noble metal inclusions in PTM, which is called metafilm strategy [74-77]. We would regard a noble metal-implanted VO_2 layer with subwavelength period of 200 nm as a tunable EMA layer with ECRIs. As depicted in the Figures 4.4(a, b), we demonstrate nanobeam (NB) and nanodisk (ND) type metafilms with various Ag filling factors, f_{Ag}. By control of geometric parameters of such inclusions, it is possible to make both increase and decrease of refractive index of PTM layer.

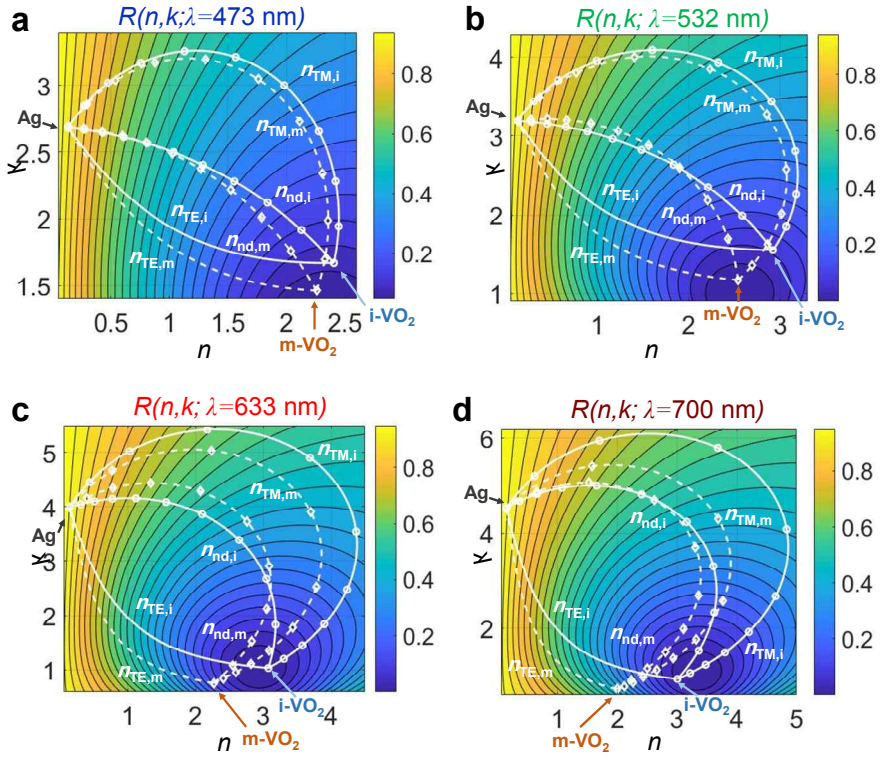

Figure 4.5 The analytic Wiener's bounds and nanodisk type effective complex refractive indices with corresponding reflection map in the (n, k) planes at the wavelevnths of (a) 473 nm (Blue), (b) 532 nm (Green), (c) 633 nm (Red), (d) 700 nm (Deep red). Reflectivity is calculated for the multilayer structure where a 40 nm-thick VO_2 layer is capped between Sapphire substrate and Ag mirror.

Our novel idea is based on the EMA and the anisotropic extraordinary properties of the Wiener's bounds while VO_2 plays a role of a tunable host material and noble plasmonic metals are implanted in it as minor inclusions.

By designing decrease and increase of ECRIs of phase-transition EMA layers, both blue and red shifts of near-unity absorption can be designed via polarization-dependent operations in NB-type metafilms. The Wiener's bounds, made of connection between two closed lines of achievable ECRI, are boundary lines of effective dielectric functions which visually reveal permitted range of ECRI when two different materials with different dielectric functions are mixed [6, 78]. The two bounds correspond to the normal and parallel effective dielectric functions, $\varepsilon_{\perp}$ and $\varepsilon_{\parallel}$, depending on filling factors of two materials which account for anisotropic dielectric function tensor of periodically layered metamaterials with subwavelength periods made of two different materials. As shown in the Fig. 4.5, the ideal theoretical approximations of $\varepsilon_{\perp}$ and $\varepsilon_{\parallel}$ are harmonic ($\varepsilon_{\perp} = (\varepsilon_1^{-1} f_1 + \varepsilon_2^{-1} f_2)^{-1}$) and arithmetic ($\varepsilon_{\parallel} = (\varepsilon_1 f_1 + \varepsilon_2 f_2)$) means of dielectric functions of constituents, respectively. In a complex dielectric function plane, correspond to circular and linear curves, respectively. The end points of the two curves correspond to complex dielectric function coordinates of two constituents. The closed region between the two bound lines can be achieved by adjusting filling factors, geometric shapes of inclusions, and incident polarization state [6, 78].

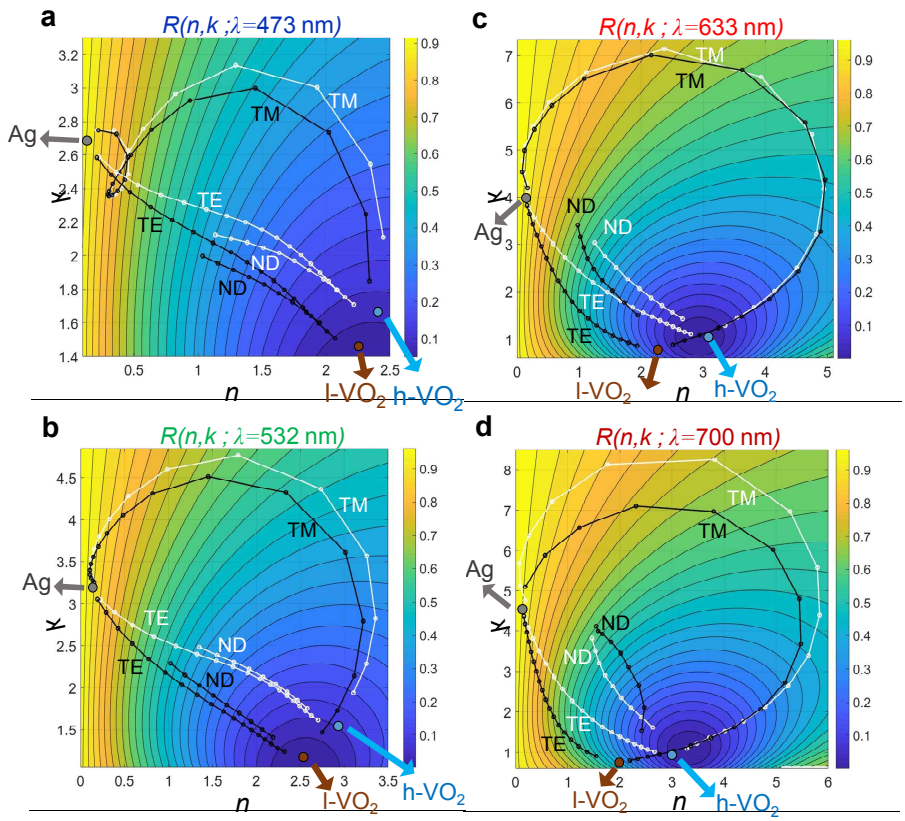

Figure 4.6 The numerically retrieved Wiener bounds of ECRIs with corresponding reflectivity maps at the four representative (a) blue, (b) green, (c) red, and (d) deep red colors. The points marked as Ag, l- VO_2, and h- VO_2 correspond to (n, k) coordinates of Ag, high index VO_2 at the insulating phase, and low index VO_2 at the metallic phase at the certain wavelengths, respectively. The white and black dotted lines denote ECRI coordinates with VO_2 at the insulating and metallic phases, respectively.

As shown in Figures 4.6(a-d), ECRIs of EMA layers in NB and ND

type metafilms are numerically retrieved for various quantities of f_{Ag} at the four representative wavelengths since it is known that real and EMA-based ideal quantities of ECRIs differ slightly in real devices according to practical geometric parameters and wavelengths [78-80]. TM and TE polarization cases of NB-type inclusions are calculated for filling factors from 0.05 to 0.95 while ECRIs of ND-type inclusions are calculated for filling factors from 0.1 to 0.5. The ECRI retrieval results show nearly similar trend of EMA theory except the blue wavelength (473 nm) (See the reference 80, Figures 4.5 and 4.6.). As f_{Ag} increases, ECRI coordinates for TM and TE polarizations, n_{TM} and n_{TE}, start to deviate from coordinates of l- VO_2 and h- VO_2 along the highly curved and nearly linear directions, respectively. For the green, red, and deep red colors, real parts of n_{TM} and n_{TE} increase and decrease, respectively, for low f_{Ag}. At the blue wavelength (473 nm), deviation of numerical retrieval results from the analytic theory is enlarged as period (200 nm) is just slightly smaller than the wavelength in sapphire substrate [74-77, 80]. It is intuitively expected that the opposite red and blue shifts of an absorption dip occur in the same NB-type metafilm with certain f_{Ag} compared to the metafilm without Ag inclusion. In case of ND-types, retrieved ECRI coordinates of them show intermediate properties slightly inclined to TE case between TM and TE cases of NB-types.

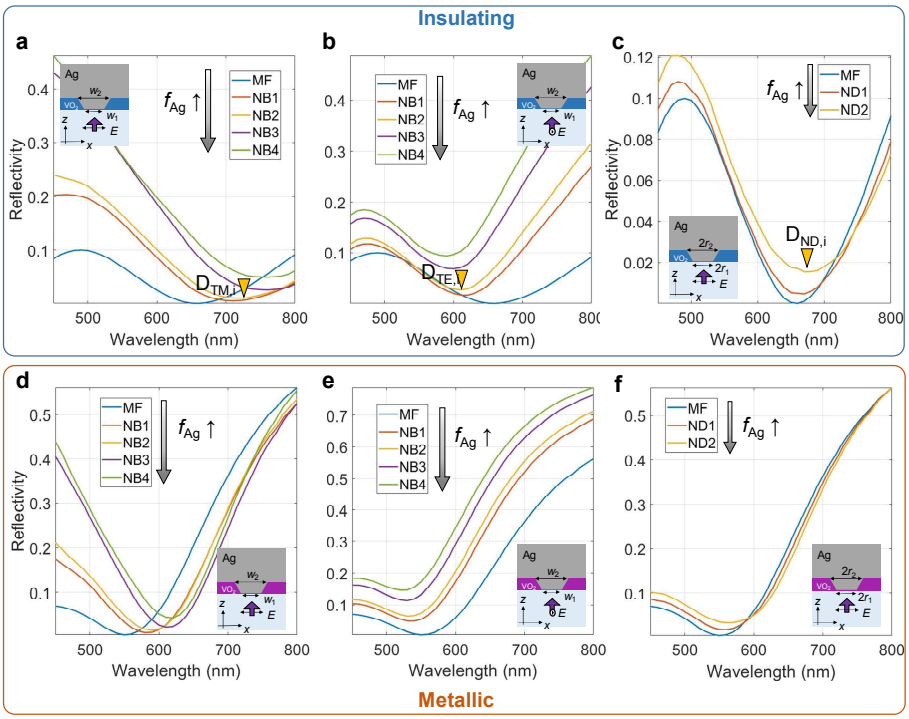

Figure 4.7 Reflectivity spectra of the NB-type and ND-type metafilms according to the increase of realizable tapered silver inclusions at the (a-c) insulating and (d-f) metallic phases of VO_2, respectively.

As shown in Figures 4.7(a-f), we investigated the four NB-type (NB1, NB2, NB3, and NB4) and two ND-type metafilms (ND1 and ND2). The f_{Ag} values of the NB-types are 0.1725 (NB1), 0.225 (NB2), 0.335 (NB3), and 0.4 (NB4), respectively, while those of the ND-types are 0.225 (ND1) and 0.35 (ND2), respectively. The corresponding parameter sets of (w_1, w_2) of NB1, NB2, NB3, and NB4 are (18 nm, 51 nm), (20 nm, 70 nm), (40 nm, 94

nm), (40 nm, 120 nm), respectively (Figures 4.7(a, b, d, and e)). The (r_1, r_2) of ND1 and ND2 are (10 nm, 40 nm) and (18 nm, 45 nm), respectively (Figures 4.7(c and f)). In Figures 4.7(a-f), designer shifts of absorption dips in the metafilms are numerically verified for NB-type and ND-type metafilms at the both insulating and metallic phases. The full-field simulations based on finite element method are conducted for infinitely periodic structures considering realistic tapering of ion beam milling process. When we compare Figures 4.7(a and b) and 4.7(d and e), polarization-dependent opposite red and blue shifts of near-unity absorption dips owing to opposite changes of ECRIs are numerically verified in NB-type metafilms. In case of ND-types in Figures 4.7(c and f), little spectral change is observed in the both phases of VO_2 as it is geometrically intermediate structure compared to NB-types.

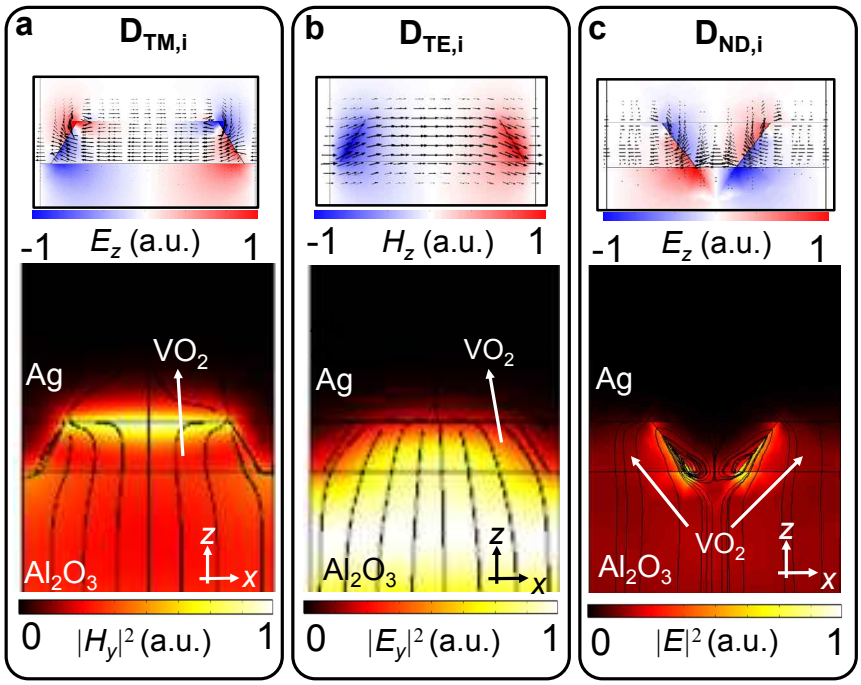

Figure 4.8 (a-c) Lower figures show normalized electromagnetic field profiles of $|H_y|^2$, $|E_y|^2$, and $|E|^2$ at the three different absorption dips at the room temperature, $D_{TM,i}$, $D_{TE,i}$, $D_{ND,i}$, which are marked in (a-c), respectively. Black lines depict the flow of Poynting vectors from the free space of Al_2O_3 to the metafilm structures. Upper figures show the E_z, H_z, and E_z with proportional black vector fields of displacement current, magnetic field, and displacement current, respectively.

The nanoscale physical origins of such tunable shifts of absorption dips which contribute to macroscopically tunable ECRIs can be explained in terms of plasmonic and Mie-like resonances. In case of TM illumination on

NB-types, Ag NBs excite SPPs at the both VO_2-Ag and Al_2O_3-Ag interfaces (Figure 4.8(a)). If f_{Ag} is low and widths (w_1 and w_2) of NB are narrow, near-unity absorption occurs at the Ag- VO_2 interface between Ag NBs as shown in Figure 4.8(a) that describes the $D_{TM,i}$. However, if w_1 and w_2 increases, funnelling into the VO_2 region between Ag NBs gets harder while SPPs oscillation at the Al_2O_3-Ag interface gets easier with increased oscillation region and SPP excitation efficiency at the interface. As refractive index of Al_2O_3 and effective SPPs mode index at the Al_2O_3-Ag interface is smaller than that of VO_2 and that at the VO_2-Ag interface, resultantly, overall effective resonance volume increases by increase of f_{Ag} in NB-type. On the other hand, as TE illumination cannot excite SPs, the only channel of light trapping and absorbing is a VO_2 region between Ag NBs via dielectric Mie-like TE resonance (Figure 4.8(b)). As a result, decreased sizes of VO_2 NBs owing to increased f_{Ag} induce decrease of effective resonator size and blue shift of resonance. In case of ND-types, localized surface plasmon resonances at the NDs contribute to the near-unity absorptions. As shown in Figure 4.8(c), incident power flow is focused on the surface of the Ag NDs at the resonance where near-fields are highly enhanced via localized SPPs.

4.2.3 Experimental demonstration

These extraordinary design and modulation of spectrum are verified experimentally. Figures 4.9 (a and b) show SEM images of the four NBs and two NDs which are designed to have the similar geometric parameters with the numerically studied structures in Figures 4.7 and 4.8. We fabricated the micron scale tiny metafilms via four steps with PLD, e-beam evaporation, and FIB milling. For measurement, we used thermo-optic micro-spectrometer setup for temperature-dependent reflectivity measurement (Figure 4.9 (c)).

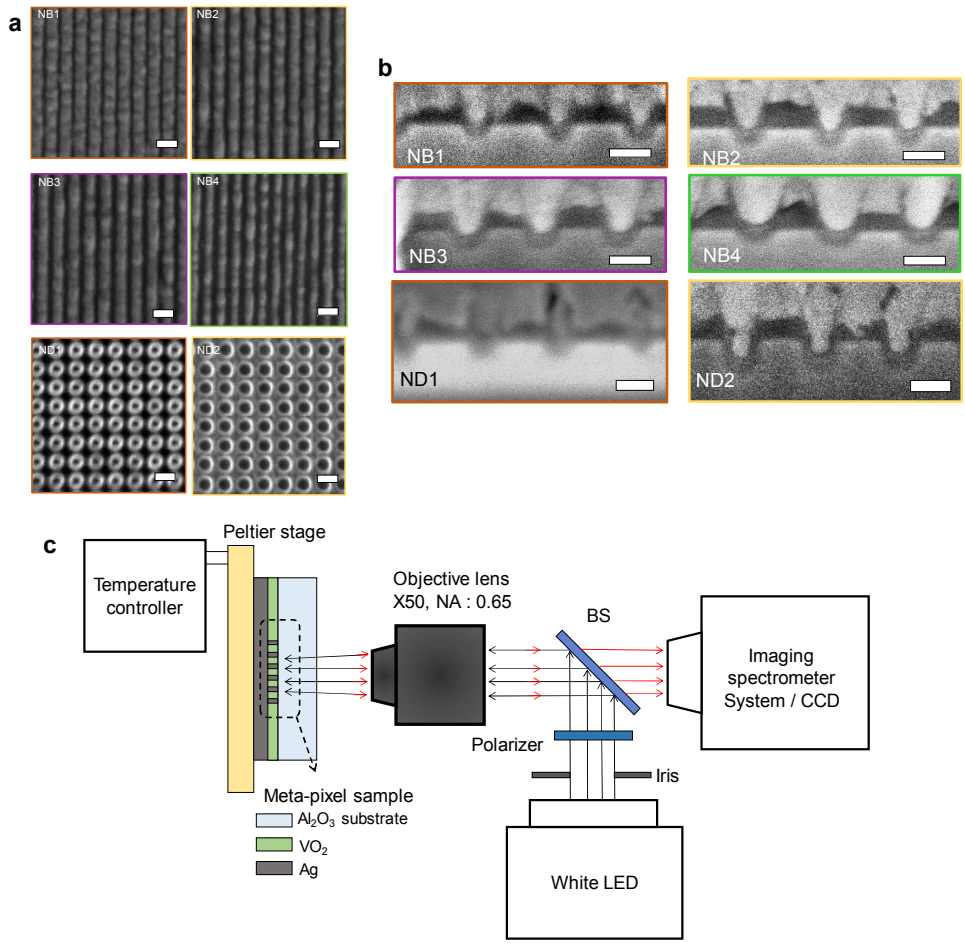

Figure 4.9 (a) SEM top view images of the NB-and ND-type metafilms. Scale bars correspond to 200 nm. (b) FIB-assisted cross-section SEM images of the fabricated NB1, NB2, NB3, NB4, ND1, and ND2 metafilm samples. The scale bars denote 100 nm. (c) Scheme of temperature-controlled bright field back scattering spectroscopy.

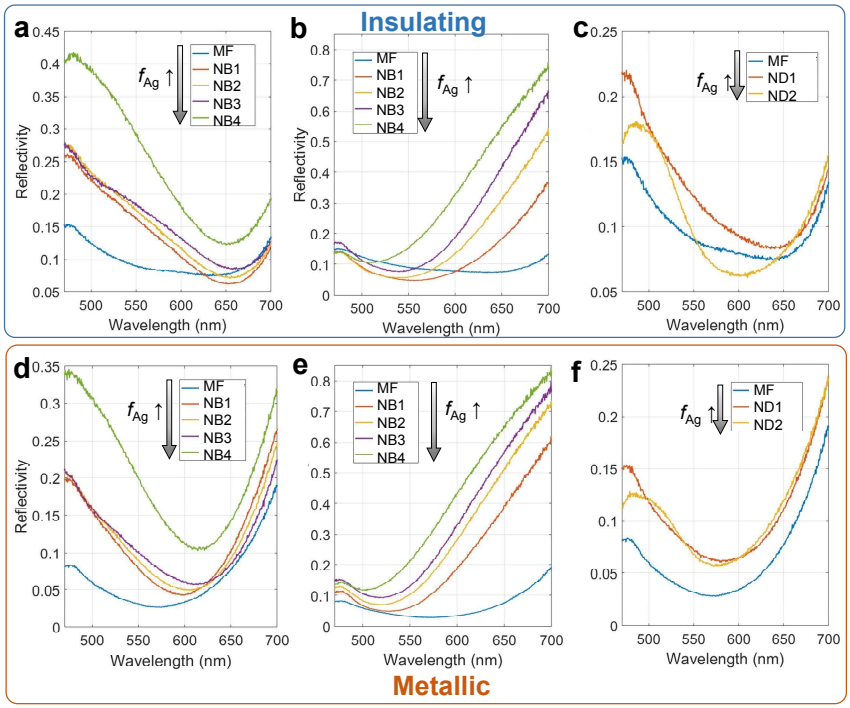
Insulating
Metallic
a
b
c
d
e
f
Reflectivity
Wavelength (nm)
f_{Ag} ↑
MF
NB1
NB2
NB3
NB4
ND1
ND2

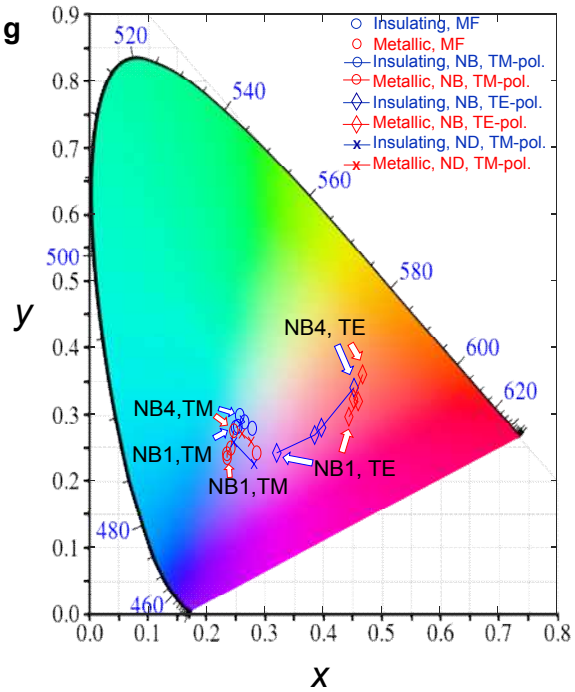
g
Insulating, MF
Metallic, MF
Insulating, NB, TM-pol.
Metallic, NB, TM-pol.
Insulating, NB, TE-pol.
Metallic, NB, TE-pol.
Insulating, ND, TM-pol.
Metallic, ND, TM-pol.
NB4, TE
NB4,TM
NB1,TM
NB1,TM
NB1, TE
x
y

Figure 4.10 Reflectivity spectra of the metafilm and six metafilm samples with the different silver inclusions at the (a-c) insulating and (d-f) metallic phases, respectively. (g) Geometry and filling factor dependencies of silver inclusion on tunable coloring at the two distinct phases described by tunable CIE coordinates.

Similar tunable trends of designer red and blue shifts of metafilms depending on geometry, polarization, and f_{Ag} are verified as shown in Figures 4.10(a-f). The wide coverage of color gamut according to HLT, f_{Ag}, geometric shape, and polarization are also verified based on the measured spectra as shown in the CIE plot of Figure 4.10(g) and Figure 4.11. Compared to Figure 4.1(h), it is shown that wider movement in the color space is enabled by the phase-transition metafilm strategy.

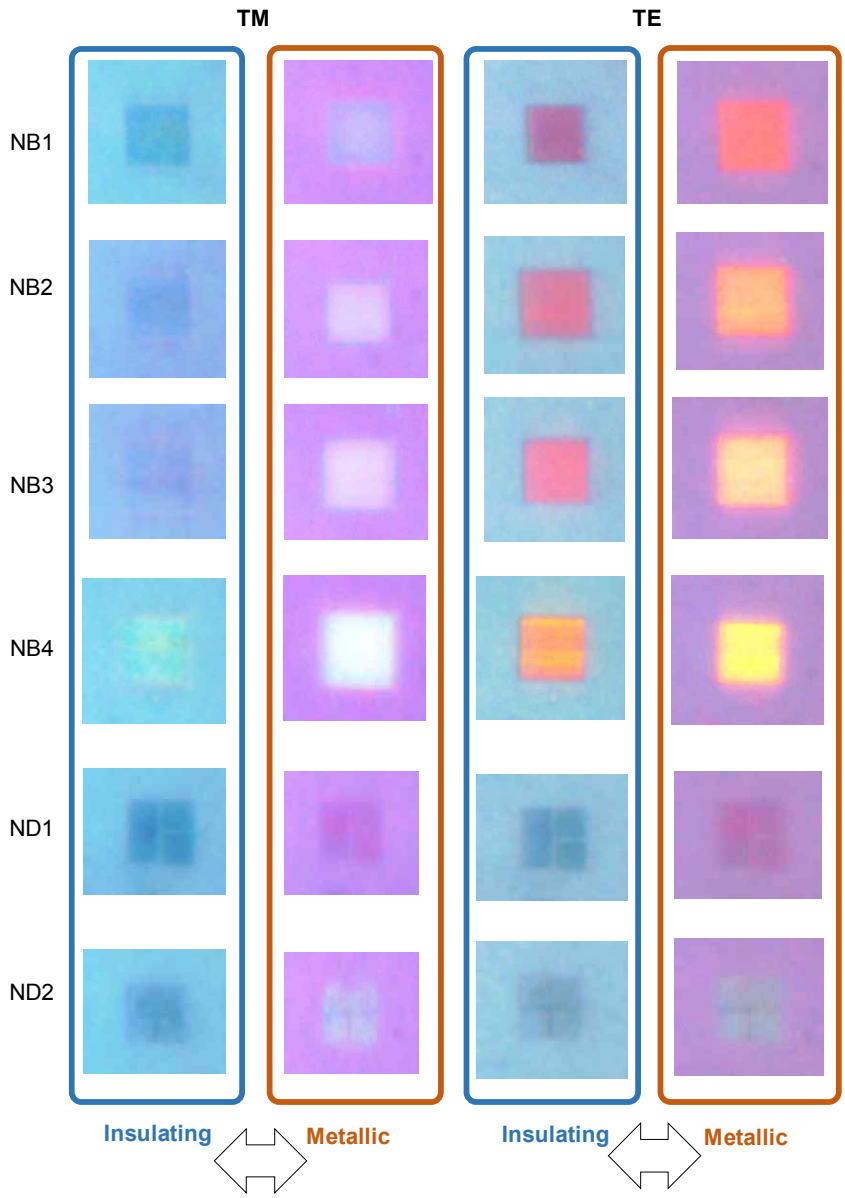

Figure 4.11 CCD images of dynamically tunable colorings at the fabricated NB and ND type metafilms for TM and TE polarized illuminations, respectively.

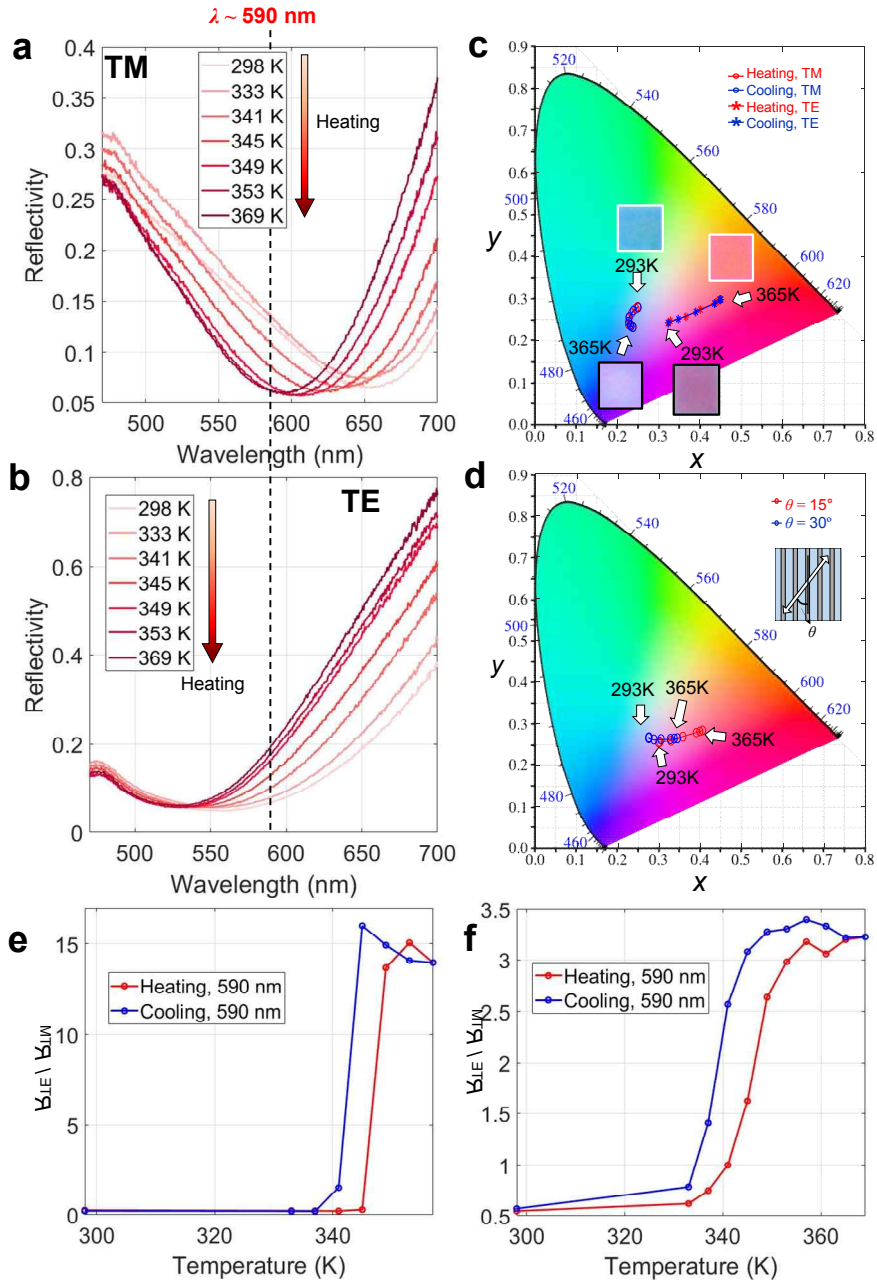

Figure 4.12 Multi-level large anisotropic responses of the NB-type metafilm with wide color generation and tunable polarization filtering. Heating induced 7-level tunable near-unity visible absorption spectra of the NB1

metafilm under illumination of (a) TM- and (b) TE-polarized light, respectively. (c) Polarization-dependent reconfigurable multi-level coloring described in CIE space. (d) Polarization rotation controlled intermediate color generations between TE and TM curves during the heating processes. The inset figure depicts top view scheme when linearly polarized light normally illuminates the NB metafilm with rotation angle, θ. Hysteresis curves of ratio between reflectivity for TE and TM polarization illumination, R_{TE}/R_{TM}, at the wavelength of 590 nm derived from (e) simulation and (f) measurement data, respectively.

The NB1 sample with f_{Ag} about 0.17 shows the best performances of near-unity absorptions for both TM and TE polarizations among the demonstrated NB-type samples. Thus, the NB1 is considered to investigate multi-level modulation of both large anisotropy and near-unity absorptions. Figures 4.12(a and b) exhibit multi-level blue and red shifts of highly anisotropic reflectivity in the NB1 sample in cases of TM and TE-polarized illuminations via thermal heating, respectively. The multi-level measurement results of the NB1 sample agree with numerical simulation results. It implies that the NB1 sample with a fixed geometry can continuously shift a near-unity absorption dip in a broad bandwidth of wavelength ranging from about 530 nm to about 670 nm by help of polarization. Under TM and TE polarizations, blue shifts of absorption dips are verified from about 670 nm

to 590 nm and from about 570 nm to 530 nm, respectively. Through the multi-level tunability, both spectrum and polarization direction of reflected light are modulated in the certain device. Figure 4.12(c) shows multi-level color generation along largely separated CIE curves according to polarization direction. Blue to light violet and orange colorings are verified experimentally under illumination of TM and TE polarizations, respectively. The intermediate color regions in a CIE space between the curves for two orthogonal polarizations can be demonstrated with intermediate polarization direction rotated from TM or TE (Figure 4.12(d)). In Figure 4.12(d), the red and blue dotted-curves correspond to the cases when polarization rotation angle, θ, is 15° and 30°, respectively. Moreover, in case of polarization state, reconfigurable tunable polarization filtering between nearly-TM and nearly-TE polarizations can be achieved at certain resonant wavelengths. When we see the orange curves of Figures 4.10 (a and b) and 4.10 (d and e), the near-unity absorption dip of the NB1 metafilm at the insulating phase for TE polarization and that at the metallic phase for TM polarization are closely met (The dip wavelengths are about 610 nm and 590 nm, respectively.). It is owing to exotic effects of NB-type silver inclusions which show the opposite ECRIs change and shifts of reflection dips according to polarization direction. At the wavelengths near those dip positions, 590 nm and 610 nm, reflectivity

is highly anisotropic. Reflection Jones matrix of a NB-type metafilm, r_{NB}, can be written as the equation (4.1).

$$r_{NB} = \begin{pmatrix} r_{TE}(\lambda, T) & 0 \\ 0 & r_{TM}(\lambda, T) \end{pmatrix} . \qquad (4.1)$$

Here, $(1\ 0)^T$ and $(0\ 1)^T$ correspond to TE and TM polarization Jones vectors while r_{TE} and r_{TM} are complex-valued reflection coefficients dependent on operation wavelength and temperature, respectively. At the wavelength of 590 nm, numerically calculated reflectivity ratio defined as $R_{TE}/R_{TM} = |r_{TE}/r_{TM}|^2$ is modulated between about 0 and 14 via heating and cooling (Figure 4.12(e)). As described in Figure 4.12(f), experimental results at the same wavelength exhibit similar trend that reflectivity ratio is modulated between about 0.5 and 3.3 in the reconfigurable manner with hysteresis.

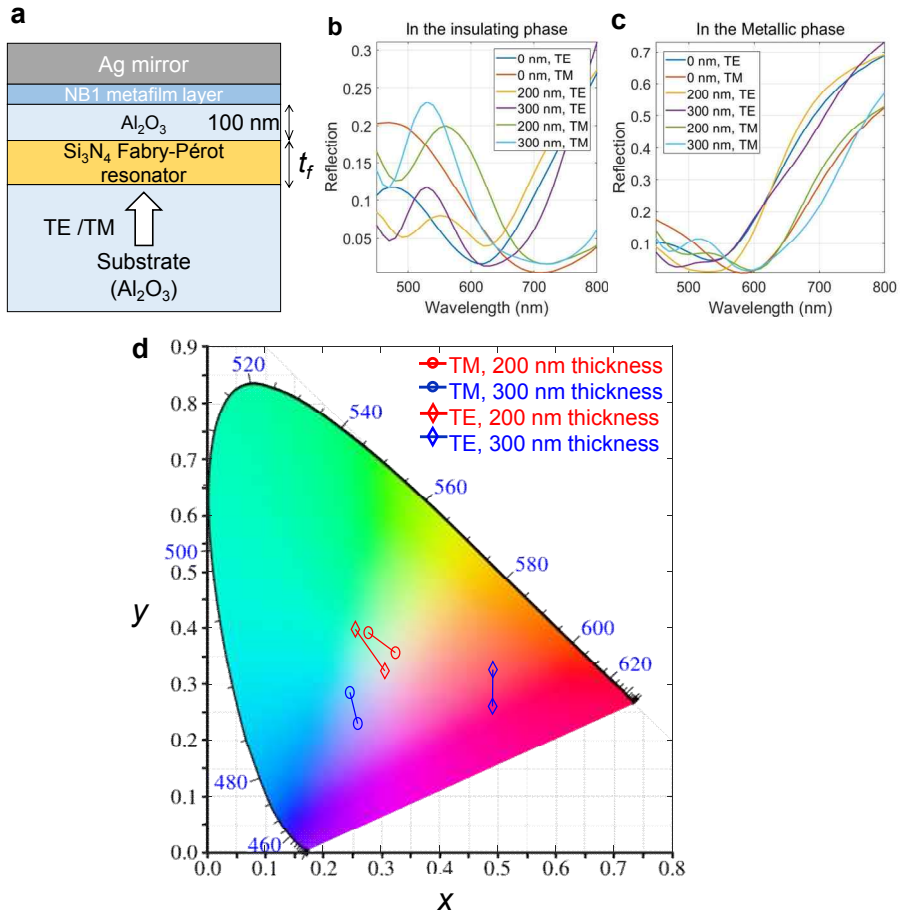

Figure 4.13 (a) Schematic illustration of the hybrid metafilm built by integrating silicon nitride film on the reflective NB1 type Ag-VO_2 metafilm. Reflection spectrum of the hybrid metafilm at the (b) insulating and (c) metallic phases, respectively. The legends in the plots denote thickness of the silicon nitride film and incident polarization state. (d) Anisotropic multifunctional tunability of color with the suggested hybrid metafilm described in the CIE space.

The compact, multifunctional, dynamically controlled phase-transition metafilm introduced so far also exhibits outstanding extensibility of designating functionality. Figure 4.13 (a) depicts an example of the hybrid metafilm composed of the absorptive phase-transition NB1 metafilm and a resonant silicon nitride film with reflection peaks. Via vertical coupling between a dynamically controlled resonantor with a low loss resonator with fixed function, thermo-optic modulation of reflection peak rather than absorption dip can be also achieved. Figures 4.13 (b and c) suggest that a reflection peak can be largely modulated according to the VO_2 phase and polarization state. Thus, multifunctional dynamic color modulation with enhanced color purity is possible in the hybrid metafilm as shown in Figure 4.13 (d). Particularly, when the thickness of silicon nitride film is set to 300 nm, high color purity modulation with large anisotropy is possible. It implies that the large area of CIE space between the TE and TM CIE curves can be also covered with adjustment of polarization direction between TE and TM.

4.3 Summary and discussions

In conclusion, inspired by strong complex interference in ultrathin lossy film and EMA theory of metamaterial, we have shown the simple and powerful framework of dynamic nanophotonics, reflective phase-transition VO_2 metafilm, working in the visible range. The proposed novel mechanism based on the polarization-dependent Wiener's bounds of an effective lossy thin film also promises an excellent potential extensibility of designing and tuning visible spectrum via stacking on other resonating films. The proposed framework would be fruitful for improvement of various integrated active optoelectronic devices including compact spatial light modulator, solar cell, photodetector, compact reflective display, and multiplexed image sensors. Moreover, it is expected that noble metal-enhanced EMA-based principles also could be a milestone research for highly integrated sub-micron active pixels with pixel-by-pixel electro-thermal control in the future when implanted inclusions deliver electrical heat into a PTM, which is one of the ultimate goals of dynamic nanophotonics.

Chapter 5 Conclusion

In this dissertation, methods for dynamic thermo-optic control of nanoscale light scattering and their applications as switch and compact modulator are discussed. The dissertation starts from conceptual introduction of dynamic nanophotonics and study of optical properties of VO_2 in Chapter 1. Then, the nanophotonic research on designing periodic arrangements and deep subwavelength geometries of VO_2 nanoantennas are proposed for various optical grating structures having deep subwavelength and over-wavelength periods. Depending on subwavelength structure of such active antennas and their arrangement period, physical working principles differ. Thus, proper theoretical explanation and design rules are mainly discussed in detail for every Chapters. Moreover, temperature-controlled performance verifications of the proposed devices are thoroughly performed through the combination of advanced nanostructure definition technologies, custom-built microscopic imaging, and spectroscopy setups.

In Chapter 2, a reconfigurable hybrid metal-VO_2 metagrating is designed and experimentally demonstrated. Individual subwavelength asymmetric nanoantenna with VO_2 is numerically designed first as a building block for directional switching of SPPs. The periodic arrangement of such

nanoantennas are demonstrated for larger SPP launching efficiency and distinction ratio based on grating period induced momentum matching. The external heating and cooling yield the IMT of VO_2 so that the directivity of transmissive SPP is switched.

In Chapter 3, to efficiently modulate forward transmission intensity of photons propagating in the free space over the broad bandwidth in the NIR, a novel phase-transition diffraction grating device is demonstrated. Basically, subwavelength light-VO_2 nanoantenna interaction is largely suppressed in the metallic phase under TE-polarized illumination owing to DPT phenomenon. On the other hand, in the insulating phase, the incident light is largely guided in VO_2 and the phase modulation effect of guided light makes destructive interference in forward diffraction when it is radiated again at the end of the nanoantenna. Resultantly, broadband characteristic of waveguiding in the insulating phase and DPT effect in the NIR, forward 0^{th} order transmission is largely modulated according to temperature control. The performance of the proposed device is predominant compared to other resonance-based active nanophotonic transmission modulators with narrow bandwidth, low efficiency, or poor modulation depth.

In Chapter 4, reflection-type phase-transition framework of VO_2 metafilm is proposed for efficient modulation of visible light spectra. The

proposed framework is based on the mirror-enhanced near-unity absorption and tuning of anisotropic effective refractive index tensor. The novel mechanism based on the polarization-dependent Wiener's bounds of an effective lossy thin PTM film suggests an excellent potential extensibility of designing and vertical integration with other multi-layered optoelectronic systems. It would ameliorate various integrated active photonic and optoelectronic devices with multifunctionality in the visible range.

I expect that this dissertation can help to develop more compact photonic elements and integrated systems based on polarization-sensitive and dynamically tunable nanoscale building blocks. I hope that this dissertation inspires research not only on VO_2-included devices but also on various PTMs with large refractive index change mediated by nanoscale application of external thermal, optical, or electrical stimuli. More elaborate demonstration of device and systems would be possible with high-resolution electron-beam lithography for definition of subwavelength patterns.

Bibliography

1. M. L. Brongersma and P. G. Kik, *Surface plasmon nanophotonics* (Springer, 2007).

2. N. I. Zheludev and Y. S. Kivshar, "From metamaterials to metadevices," Nat. Mater. **11**(11), 917-924 (2012).

3. S. A. Maier, *Plasmonics: fundamentals and applications* (Springer Science & Business Media, 2007).

4. W. L. Barnes, A. Dereux, and T. W. Ebbesen, "Surface plasmon subwavelength optics," Nature **424**(6950), 824-830 (2003).

5. T. W. Ebbesen, H. J. Lezec, H. F. Ghaemi, T. Thio, and P. A. Wolff, "Extraordinary optical transmission through sub-wavelength hole arrays," Nature **391**(6668), 667-669 (1998).

6. W. Cai and V. Shalaev, *Optical metamaterials: fundamentals and applications* (Springer Science & Business Media, 2009).

7. H. J. Lezec, J. A. Dionne, and H. A. Atwater, "Negative refraction at visible frequencies," Science **316**(5823), 430-432 (2007).

8. W. Cai, U. K. Chettiar, A. V. Kildishev, and V. M. Shalaev, "Optical cloaking with metamaterials." Nat. Photon. **1**(4), 224-227 (2007).

9. M. Ferrera, N. Kinsey, A. Shaltout, C. DeVault, V. Shalaev, and A. Boltasseva, "Dynamic nanophotonics," JOSA B **34**(1), 95-103 (2017).

10. I. V. Shadrivov, M. Lapine, and Y. S. Kivshar, *Nonlinear, tunable and active metamaterials* (Springer, 2015).

11. P. Lalanne and P. Chavel, "Metalenses at visible wavelengths: past, present, perspectives," Laser & Photon. Rev., **11**(3), 1600295 (2017).

12. L. Novotny and N. Van Hulst, "Antennas for light," Nat. Photon. **5**(2), 83-90 (2011).

13. Saleh, B. E., Teich, M. C., & Saleh, B. E. (1991). *Fundamentals of photonics* (Vol. 22). New York: Wiley.

14. A. N. Grigorenko, M. Polini, and K. S. Novoselov, "Graphene plasmonics," Nat. Photon. **6**(11), 749-758 (2012).

15. J. A. Dionne, K. Diest, L. A. Sweatlock, and H. A. Atwater, "PlasMOStor: a metal− oxide− Si field effect plasmonic modulator," Nano Lett. **9**(2), 897-902 (2009).

16. X. Duan, S. Kamin, and N. Liu, "Dynamic plasmonic colour

display," Nat. Commun. **8**, 14606 (2017).

17. J. Li, S. Kamin, G. Zheng, F. Neubrech, S. Zhang, and N. Liu, "Addressable metasurfaces for dynamic holography and optical information encryption," Sci. Adv. **4**(6), eaar6768 (2018).

18. M. M. Qazilbash *et al*., "Electrodynamics of the vanadium oxides V O_2 and V_2O_3," Phys. Rev. B, **77**(11), 115121 (2008).

19. J. W. Park *et al*. "Optical properties of pseudobinary GeTe, $Ge_2Sb_2Te_5$, $GeSb_2Te_4$, $GeSb_4Te_7$, and Sb_2Te_3 from ellipsometry and density functional theory," Phys. Rev. B ***80***(11), 115209 (2009).

20. M. A. Mroginski, N. E. Massa, H. Salva, J. A. Alonso, and M. J. Martínez-Lope, "Metal-insulator phase transitions of $SmNiO_3$ and $PrNiO_3$: Electrons in a polaronic medium," Phys. Rev. B **60**(8), 5304 (1999).

21. H.-T. Kim *et al*. "Mechanism and observation of Mott transition in VO_2-based two- and three-terminal devices," New J. Phys. **6**, 52–70 (2004).

22. F. J. Morin, "Oxides which show a metal-to-insulator transition at the Neel temperature," Phys. Rev. Lett. **3**(1), 34 (1959).

23. J. M. Baik *et al*., "Pd-Sensitized single vanadium oxide nanowires: highly responsive hydrogen sensing based on the metal− insulator transition," Nano Lett., **9**(12), 3980-3984 (2009).

24. D. Ruzmetov, G. Gopalakrishnan, C. Ko, V. Narayanamurti, and S. Ramanathan, "Three-terminal field effect devices utilizing thin film vanadium oxide as the channel layer," J. Appl. Phys. **107**(11), 114516 (2010).

25. T. Driscoll *et al*., "Memory metamaterials," Science, **325**(5947), 1518-1521 (2009).

26. M. Seo *et al*., "Active terahertz nanoantennas based on VO_2 phase transition," Nano Lett. **10**(6), 2064-2068 (2010).

27. M. J. Dicken *et al*., "Frequency tunable near-infrared metamaterials based on VO_2 phase transition," Opt. Express **17**(20), 18330-18339 (2009).

28. T. Huang *et al*., "Study of the phase evolution, metal-insulator transition, and optical properties of vanadium oxide thin films," Opt. Mater. Express **6**(11), 3609-3621 (2016).

29. E. Devaux, T. W. Ebbesen, J. C. Weeber, and A. Dereux,

"Launching and decoupling surface plasmons via micro-gratings," Appl. Phys. Lett., **83**(24), 4936-4938 (2003).

30. F. López-Tejeira *et al*., "Efficient unidirectional nanoslit couplers for surface plasmons," Nat. Phys. **3**(5), 324-328 (2007).

31. J. Lin *et al*., "Polarization-controlled tunable directional coupling of surface plasmon polaritons," Science **340**(6130), 331-334 (2013).

32. S. Y. Lee *et al*., "Role of magnetic induction currents in nanoslit excitation of surface plasmon polaritons," Phys. Rev. Lett. **108**(21), 213907 (2012).

33. S. Y. Lee, K. Kim, S.-J. Kim, H. Park, K. Y. Kim, and B. Lee, "Plasmonic meta-slit: shaping and controlling near-field focus," Optica **2**(1), 6-13 (2015).

34. J. Chen *et al*., "Efficient unidirectional generation of surface plasmon polaritons with asymmetric single-nanoslit," Appl. Phys. Lett. **97**(4), 041113 (2010).

35. L. Huang *et al*., "Helicity dependent directional surface plasmon polariton excitation using a metasurface with interfacial phase discontinuity," Light: Sci. & Appl. **2**(3), e70 (2013).

36. A. Pors, M. G. Nielsen, T. Bernardin, J. C. Weeber, and S. I. Bozhevolnyi, "Efficient unidirectional polarization-controlled excitation of surface plasmon polaritons," Light: Sci. & Appl. **3**(8), e197 (2014).

37. J. B. Mueller, K. Leosson, and F. Capasso, "Polarization-selective coupling to long-range surface plasmon polariton waveguides," Nano Lett. **14**(10), 5524-5527 (2014).

38. K. F. MacDonald and N. I. Zheludev, "Active plasmonics: current status," Laser & Photon. Rev. **4**(4), 562-567 (2010).

39. H. Mühlenbernd *et al*. "Amplitude-and phase-controlled surface plasmon polariton excitation with metasurfaces." ACS Photonics **3**(1), 124-129 (2016).

40. U. Efron, *Spatial light modulator technology: materials, devices, and applications* (CRC press, 1994).

41. C. Argyropoulos, "Enhanced transmission modulation based on dielectric metasurfaces loaded with graphene," Opt. Express **23**(18), 23787-23797 (2015).

42. G. D. Liu, X. Zhai, S. X. Xia, Q. Lin, C. J. Zhao, and L. L. Wang, "Toroidal resonance based optical modulator employing hybrid

graphene-dielectric metasurface," Opt. Express **25**(21), 26045-26054 (2017).

43. S. Kim, M. S. Jang, V. W. Brar, Y. Tolstova, K. W. Mauser, and H. A. Atwater, "Electronically tunable extraordinary optical transmission in graphene plasmonic ribbons coupled to subwavelength metallic slit arrays," Nat. Commun. **7**, 12323 (2016).
44. A. Howes, W. Wang, I. Kravchenko, and J. Valentine, "Dynamic transmission control based on all-dielectric Huygens metasurfaces," Optica **5**(7), 787-792 (2018).
45. J. Park, J. H. Kang, X. Liu, and M. L. Brongersma, "Electrically tunable epsilon-near-zero (ENZ) metafilm absorbers," Sci. Rep. **5**, 15754 (2015).
46. X. Liu, J. H. Kang, H. Yuan, J. Park, Y. Cui, H. Y. Hwang, and M. L. Brongersma, "Tuning of Plasmons in Transparent Conductive Oxides by Carrier Accumulation," ACS Photonics **5**(4), 1493-1498 (2018).
47. P. P. Iyer, M. Pendharkar, and J. A. Schuller, "Electrically reconfigurable metasurfaces using heterojunction resonators," Adv. Opt. Mater. **4**(10), 1582-1588 (2016).

48. M. Rahmani, L. Xu, A. E. Miroshnichenko, A. Komar, R. Camacho‐Morales, H. Chen, Y. Zarate, S. Kruk, G. Zhang, D. N. Neshev, and Y. S. Kivshar, "Reversible Thermal Tuning of All‐Dielectric Metasurfaces," Adv. Funct. Mater. **27**(31), 1700580 (2017).

49. M. D. Goldflam, M. K. Liu, B. C. Chapler, H. T. Stinson, A. J. Sternbach, A. S. McLeod, J. D. Zhang, K. Geng, M. Royal, B.-J. Kim, R. D. Averitt, N. M. Jokerst, D. R. Smith, H.-T. Kim, and D. N. Basov, "Voltage switching of a VO_2 memory metasurface using ionic gel," Appl. Phys. Lett. **105**(4), 041117 (2014).

50. N. A. Butakov, M. W. Knight, T. Lewi, P. P. Iyer, D. Higgs, H. T. Chorsi, J. Trastoy, J. D. V. Granda, I. Valmianski, C. Urban, Y. Kalcheim, P. Y. Wang, P. W. C. Hon, I. K. Schuller, and J. A. Schuller, "Broadband Electrically Tunable Dielectric Resonators Using Metal-Insulator Transitions," ACS Photonics (2018).

51. K. Appavoo and R. F. Haglund Jr, "Polarization selective phase-change nanomodulator," Sci. Rep. **4**, 6771 (2014).

52. E. U. Donev, J. Y. Suh, F. Villegas, R. Lopez, R. F. Haglund Jr, and L. C. Feldman, "Optical properties of subwavelength hole arrays in vanadium dioxide thin films," Phys. Rev. B **73**(20), 201401 (2006).

53. S.-J. Kim, H. Yun, K. Park, J. Hong, J.-G. Yun, K. Lee, J. Kim, S. J. Jeong, S.-E. Mun, J. Sung, Y. W. Lee, and B. Lee, "Active directional switching of surface plasmon polaritons using a phase transition material," Sci. Rep. **7**, 43723 (2017).

54. X. Liu, J. Liang, N. Li, and M. Wu, "Preparation of paraboloid-like VO_2@ SiO_2 nanostructured arrays for enhanced transmission," Mater. Lett. **160**, 585-588 (2015).

55. İ. Karakurt, J. Boneberg, P. Leiderer, R. Lopez, A. Halabica, and R. F. Haglund Jr, "Transmission increase upon switching of VO_2 thin films on microstructured surfaces," Appl. Phys. Lett. **91**(9), 091907 (2007).

56. E. U. Donev, J. Y. Suh, R. Lopez, L. C. Feldman, and R. F. Haglund Jr, "Using a semiconductor-to-metal transition to control optical transmission through subwavelength hole arrays," Adv. Optoelectron. **2008**, 739135, (2008).

57. H. Matsui, Y. L. Ho, T. Kanki, H. Tanaka, J. J. Delaunay, and H. Tabata, "Mid‐ infrared Plasmonic Resonances in 2D VO_2 Nanosquare Arrays," Adv. Opt. Mater. **3**(12), 1759-1767 (2015).

58. Q. Wang, E. T. Rogers, B. Gholipour, C. M. Wang, G. Yuan, J. Teng, and N. I. Zheludev, "Optically reconfigurable metasurfaces

and photonic devices based on phase change materials," Nat. Photon. **10**(1), 60 (2016).

59. B. Gholipour, A. Karvounis, J. Yin, C. Soci, K. F. MacDonald, and N. I. Zheludev, "Phase-change-driven dielectric-plasmonic transitions in chalcogenide metasurfaces," NPG Asia Mater. **10**, 533-539 (2018).
60. A. V. Pogrebnyakov, J. A. Bossard, J. P. Turpin, J. D. Musgraves, H. J. Shin, C. Rivero-Baleine, N. Podraza, K. A. Richardson, D. H. Werner, and T. S. Mayer, "Reconfigurable near-IR metasurface based on $Ge_2Sb_2Te_5$ phase-change material," Opt. Mater. Express **8**(8), 2264-2275 (2018).
61. C. Choi, S.-J. Kim, J.-G. Yun, J. Sung, S.-Y. Lee, and B. Lee, "Deflection angle switching with a metasurface based on phase-change nanorods," Chin. Opt. Lett. **16**(5), 050009 (2018).
62. E. Petronijevic and C. Sibilia, "All-optical tuning of EIT-like dielectric metasurfaces by means of chalcogenide phase change materials," Opt. Express **24**(26), 30411-30420 (2016).
63. J. Tian, Q. Li, J. Lu, and M. Qiu, "Reconfigurable all-dielectric antenna-based metasurface driven by multipolar resonances," Opt. Express **26**(18), 23918-23925 (2018).

64. Z. Li, Y. Zhou, H. Qi, Q. Pan, Z. Zhang, N. N. Shi, M. Lu, A. Stein, C. Y. Li, S. Ramanathan, and N. Yu, "Correlated Perovskites as a - Tunable Photonics," Adv. Mater. **28**(41), 9117-9125 (2016).

65. M. Khorasaninejad and F. Capasso, "Broadband multifunctional efficient meta-gratings based on dielectric waveguide phase shifters," Nano Lett. **15**(10), 6709-6715 (2015).

66. M. Khorasaninejad, F. Aieta, P. Kanhaiya, M. A. Kats, P. Genevet, D. Rousso, and F. Capasso, "Achromatic metasurface lens at telecommunication wavelengths," Nano Lett. **15**(8), 5358-5362 (2015).

67. M. Khorasaninejad, W. Zhu, and K. B. Crozier, "Efficient polarization beam splitter pixels based on a dielectric metasurface," Optica **2**(4), 376-382 (2015).

68. J. Rensberg, S. Zhang, Y. Zhou, A. S. McLeod, C. Schwarz, M. Goldflam, M. Liu, J. Kerbusch, R. Nawrodt, S. Ramanathan, D. N. Basov, F. Capasso, C. Ronning, and M. A. Kats, "Active optical metasurfaces based on defect-engineered phase-transition materials," Nano Lett. **16**(2), 1050-1055 (2016).

69. Y. Horie, A. Arbabi, E. Arbabi, S. M. Kamali, and A. Faraon,

"High-speed, phase-dominant spatial light modulation with silicon-based active resonant antennas," ACS Photonics **5**(5), 1711-1717 (2017).

70. W. W. Salisbury, "Absorbent body for electromagnetic waves," U.S. Patent No. 2,599,944 (1952).

71. R. L. Fante and M. T. Mccormack, "Reflection properties of the Salisbury screen," IEEE Trans. Antennas Propag. **36**(10), 1443-1454 (1988).

72. M. A. Kats *et al*., "Ultra-thin perfect absorber employing a tunable phase change material," Appl. Phys. Lett. **101**(22), 221101 (2012).

73. M. A. Kats, R. Blanchard, P. Genevet, and F. Capasso, "Nanometre optical coatings based on strong interference effects in highly absorbing media," *Nat. Mater*. **12**(1), 20-24 (2013).

74. S. J. Kim, P. Fan, J. H. Kang, and M. L. Brongersma, "Creating semiconductor metafilms with designer absorption spectra," Nat. Commun. **6**, 7591 (2015).

75. S. J. Kim, J. Park, M. Esfandyarpour, E. F. Pecora, P. G. Kik, and M. L. Brongersma, "Superabsorbing, artificial metal films constructed

from semiconductor nanoantennas," Nano Lett. **16**(6), 3801-3808 (2016).

76. M. Esfandyarpour, E. C. Garnett, Y. Cui, M. D. McGehee, and M. L. Brongersma, "Metamaterial mirrors in optoelectronic devices," Nat. Nanotechnol. **9**(7), 542-547 (2014).
77. P. Wang, A. V. Krasavin, M. E. Nasir, W. Dickson, and A. V. Zayats, "Reactive tunnel junctions in electrically driven plasmonic nanorod metamaterials," Nat. Nanotechnol. **13**(2), 159-164 (2018).
78. O. Wiener, "Zur Theory der Refraktionskonstanten Abh," Math Phys. K1 Königl. Sächs. Ges, **32**, 509 (1912).
79. A. Fang, T. Koschny, and C. M. Soukoulis, "Optical anisotropic metamaterials: Negative refraction and focusing," Phys. Rev. B **79**, 245127 (2009).
80. D. R. Smith, D. C. Vier, T. Koschny, and C. M. Soukoulis, "Electromagnetic parameter retrieval from inhomogeneous metamaterials," Phys. Rev. E **71**, 036617 (2005).

Appendix

Portions of the work discussed in this dissertation are also published in the following publication:

[Chapter 1, 3] S.-J. Kim, S. Choi, C. Choi, Y. Lee, J. Sung, H. Yun, J. Jeong, S.-E. Mun, Y. W. Lee, and B. Lee, "Broadband efficient modulation of light transmission with high contrast using reconfigurable VO_2 diffraction grating," Optics Express, 2018 (accepted).

[Chapter 2] S.-J. Kim, H. Yun, K. Park, J. Hong, J.-G. Yun, K. Lee, J. Kim, S. J. Jeong, S.-E. Mun, J. Sung, Y. W. Lee, and B. Lee, "Active directional switching of surface plasmon polaritons using a phase transition material," Scientific Reports, vol. 7, article 43723, DOI: 10.1038/srep43723, 2017.

Portions of the work discussed in this dissertation are also submitted to the international journals as follows:

[Chapter 1, 4] S.-J. Kim, H. Yun, S. Choi, J.-G. Yun, K. Park, S. J. Jeong, S.-Y. Lee, Y. Lee, J. Sung, C. Choi, J. Hong, Y. W. Lee, and B. Lee, " Noble metal-enhanced absorbing phase-transition metafilm for multifunctional modulation of visible light," Laser & Photonics Reviews, 2018 (submitted).

초 록

지난 약 20년간 다양한 형태의 나노광학 소자들이 플라즈모닉스와 메타물질 기술들을 통해 개발되어 왔다. 이러한 소자들의 주된 목표는 금속 표면에 빛을 집속함으로써 기존 벌크 광학 소자들의 기능을 파장 한계 이하로 소형화된 스케일에서 구현하거나, 자연에 없는 특성을 보이는 광학적 물질을 개발하는 것이다. 이를 통하여 궁극적으로 차세대 초소형 고집적 광학 시스템을 만드는 것이 두 분야의 주요한 목표이다. 특히, 유전 함수 스펙트럼이 외부 자극에 의해 조절이 가능한 능동 물질과 나노광학 소자의 결합을 통해 능동적으로 외부 자극에 의해 기능이 변조되는 나노광학 소자들에 대한 연구들이 큰 주목을 받아왔다.

최근에 대표적인 절연체-금속 상변이 물질인 바나듐이산화물을 이용한 나노광학 소자 개발이 주목 받고 있다. 바나듐이산화물은 가시광선, 근적외선 및 적외선 파장 대역에서 온도에 따라 큰 폭의 유전 함수 변화가 일어난다는 장점이 있다.

본 박사학위 논문에서는 주기적으로 배열된 광 격자 구조들에 바나듐이산화물을 결합하여 입사광의 산란 양상을 큰 폭으로 조절하는 새로운 공학적 응용 방법들을 제안한다. 바나듐이산화물의 상변이를 이용하여 산란된 가시광선 및 근적외선의 운동량, 세기, 스펙트럼, 그리고 편광을 효율적으로 조절하는 새로운 방법들을 개발하였다. 각 장 별로 제안한 광소자의 목적 및 동작 대역에 따라서 격자의 주기, 구성 물질 및 구조를 설계하는 이론 및 전산모사 연구를 수행하고 이를 실험적으로 검증한다.

첫번째 장에서는, 능동 나노광학에 대한 간략한 소개와 함께 바나듐이산화물의 유전 함수 변화를 중심으로 동작 파장 대역에 따른 상변이 현상의 특성을 논한다. 다음으로는 금속 표면 위에 집속된 빛의 형태인 표면 플라즈몬 폴라리톤을 여기하고 그 방향을 뒤바꾸는 상변이 광 스위치를 제안한다. 열에 의해 뒤바뀌는 비대칭 나노안테나와 파장 이하 광학 격자에 의한 운동량 보상에 기반하여 표면 플라즈몬 폴라리톤의 방향성이 크게 변함을 보인다.

세번째 장에서는, 광대역에서 비공진 작동이 가능한 직진 광 투과율 조절기를 바나듐 이산화물 격자를 통해 구현한다. 근적외선 대역에서 나타나는 유전체-플라즈모닉 상변이 특성과 나노 도파로에 의한 광대역 초소형 간섭계 구조에 기반하여 고성능 능동 투과율 변조가 가능함을 보인다.

네번째 장에서는, 가시광선의 색 스펙트럼과 편광 방향을 효율적으로 조절하는 바나듐이산화물 메타필름 연구를 소개한다. 반사형 구조의 완전 흡수 현상과 유효 매질 이론을 통한 편광 의존적 유효 굴절률의 설계를 활용한, 가시광선의 효율적인 능동 변조 프레임워크를 제시한다.

마지막으로 결론에서는 연구 결과들의 요약과 그 가치에 대한 논의로 학위논문을 마무리 한다. 본 박사학위 논문의 결과는 능동적 변조가 요구되는 차세대 초소형 광 스위치, 초소형 디스플레이 픽셀, 공간 광 변조기 등에 기여할 수 있을 것으로 기대된다.

주요어: 나노광학, 능동 광 조절, 상변이 물질, 바나듐이산화물, 나노광격자, 메타물질
학 번: 2014-21652